This Work has not yet been peer-reviewed and is provided by the contributing Author(s) as a means to ensure timely dissemination of scholarly and technical Work on a noncommercial basis. Copyright and all rights therein are maintained by the Author(s) or by other copyright owners. It is understood that all persons copying this information will adhere to the terms and constraints invoked by each Author's copyright. This Work may not be reposted without explicit permission of the copyright owner. This work has been submitted to the Journal of Physical Oceanography. Copyright in this work may be transferred without further notice.

# Submesoscale dynamics of dense overflows.

# Part I: Potential vorticity fluxes and symmetric instability

Victoria Whitley,[a] Jacob Wenegrat,[a,b] and Leif Thomas[c]

[a] *Applied Mathematics & Statistics, and Scientific Computation Program, University of Maryland, College Park*

[b] *Department of Atmospheric and Oceanic Science, University of Maryland, College Park*

[c] *Department of Earth System Science, Stanford University*

*Corresponding author*: Victoria Whitley, vicwhit28@gmail.com

ABSTRACT: Dense overflows descending from continental shelves are a key component of the global overturning circulation, yet the submesoscale processes that shape their potential vorticity (PV) structure and drive cross-shelf exchange remain poorly understood. This study uses a three-dimensional large-eddy simulation of a dense overflow to examine how surface cooling and the descending gravity current set the PV structure of the overflow and precondition the shelf for symmetric instability (SI). Surface cooling generates a geostrophically balanced, along-slope flow and topography-aligned isopycnals, while the descending gravity current injects positive PV at the shelf break that is then advected down the slope, capping the overflow with elevated PV in the stratified interior. This high PV contrasts with previous overflow simulations, which found thin bands of negative PV in the interior and attributed them to SI. Here the resolved bottom PV injection keeps the interior symmetrically stable. Instead, SI is only found on the shelf where surface cooling leaves a negative PV anomaly. The resulting SI cells propagate toward the shelf break, driving episodic subinertial off-shelf export of dense water. Together, these results show that boundary PV fluxes generated by dense overflows can control cross-shelf export and a lasting interior PV signature within deep boundary currents, with implications for representing water-mass transformation in the ocean overturning circulation. This is part I of II, with the companion paper focusing on how this background structure modifies the propagation of near-inertial waves.

## 1. Introduction

Gravity-driven currents descending from marginal seas and high-latitude shelves, known as dense overflows, play a crucial role in the global overturning circulation (Killworth 1983; Lumpkin and Speer 2007). Buoyancy loss from cooling as well as brine rejection (most common in some regions in the Southern Ocean) during sea-ice formation produces dense, well-ventilated waters that descend along sloping topography, transporting oxygen, carbon, and nutrient-rich water into the deep ocean, while entraining warmer ambient water (Killworth 1983; Lumpkin and Speer 2007; Bullister et al. 2013). Dense overflows from the Denmark Strait, Labrador Sea, and Iceland-Scotland Ridge are fundamental to the formation of North Atlantic Deep Water and therefore the Atlantic Meridional Overturning Circulation (Dickson and Brown 1994; Lumpkin and Speer 2007; Almansi et al. 2017; Evans et al. 2022). Similar dense overflows occur globally, including in the Mediterranean, Red, Ross, and Weddell Seas, where they transport deep and intermediate dense water (Killworth 1983; Lumpkin and Speer 2007; Legg 2012). The properties of these water masses are strongly shaped by localized mixing along dense overflow pathways, yet the influence of submesoscale instabilities and internal wave–mean flow interactions on their mean flow remains poorly understood (Magaldi and Haine 2015; Yankovsky and Legg 2019). Understanding the physical mechanisms that can govern water-mass transformation and their coupling to other dynamical pathways is therefore essential for accurately representing large-scale ocean circulation, improving global models, and informing climate projections.

Dense overflows can be associated with conditions favorable to symmetric instability (SI), a submesoscale overturning instability which occurs when the Ertel potential vorticity (PV) and the absolute vorticity take the opposite and same sign of the Coriolis parameter, respectively, and the stratification is stable (Haine and Marshall 1998; Thomas et al. 2013). These conditions can readily be produced by surface cooling that generates dense overflows. Observational evidence of SI in dense water formation and overflow regions continues to grow (Brearley et al. 2012; Naveira Garabato et al. 2019; Lin et al. 2020; Le Bras et al. 2022), with some model studies also inferring its presence in the deep boundary currents generated by dense overflows (Yankovsky and Legg 2019). Indeed, parameterizing SI improves the representation of water-mass transformation in coarse-resolution overflow models (Yankovsky et al. 2021), pointing to a dynamically important

role; yet how SI shapes the cross-shelf exchange of newly formed dense water has not been established.

This study examines how the flow and stratification shaped by dense overflows set the PV structure of the overflow and, in turn, precondition it for SI and cross-shelf export. Large-eddy simulation (LES) of a dense overflow system captures key small-scale dynamics during overflow formation, propagation, and the subsequent evolution once cooling is removed and the gravity current adjusts. These simulated stages are representative of the temporal variability of realistic dense overflows (Köhl et al. 2007; Magaldi et al. 2011; Chafik et al. 2023). Surface cooling initiates overflow formation and establishes a mean geostrophic, along-isobath flow field with sloping isopycnals. While surface cooling reduces PV, the PV budget used in this analysis indicates the downslope currents also inject PV along the bottom, capping the overflow with layered bands of high PV interspersed with lower but positive PV and leaving the stratified interior symmetrically stable; only on the shelf does the cooling-driven negative PV anomaly support SI. There, SI organizes into slantwise overturning cells that propagate offshore and deliver pulses of dense shelf water to the shelf break, producing episodic, subinertial off-shelf export that would not otherwise occur. The resolved shelf SI and bottom PV injection diagnosed here offer a mechanistic understanding of the enhanced off-shelf transport and water-mass transformation that has been parameterized in coarse-resolution overflow models (Yankovsky et al. 2021). The simulations also distinguish genuine shelf SI from symmetrically stable, banded shear structures in the interior, which a companion paper shows are attributable to interactions between near-inertial waves (NIWs) and the baroclinic flow (Whitley et al. 2026).

The paper is organized as follows. Section 2 describes the numerical configuration used to generate the dense overflow. Section 3 presents the evolution and dynamical behavior of the overflow, including its transition after cooling is shut off. Section 4 examines the PV budget and the associated boundary fluxes at each stage. Section 5 characterizes the shelf SI behavior and its influence on cross-shelf exchange. Section 6 discusses these findings in the context of previous overflow studies, and Section 7 summarizes the conclusions and implications for future work.

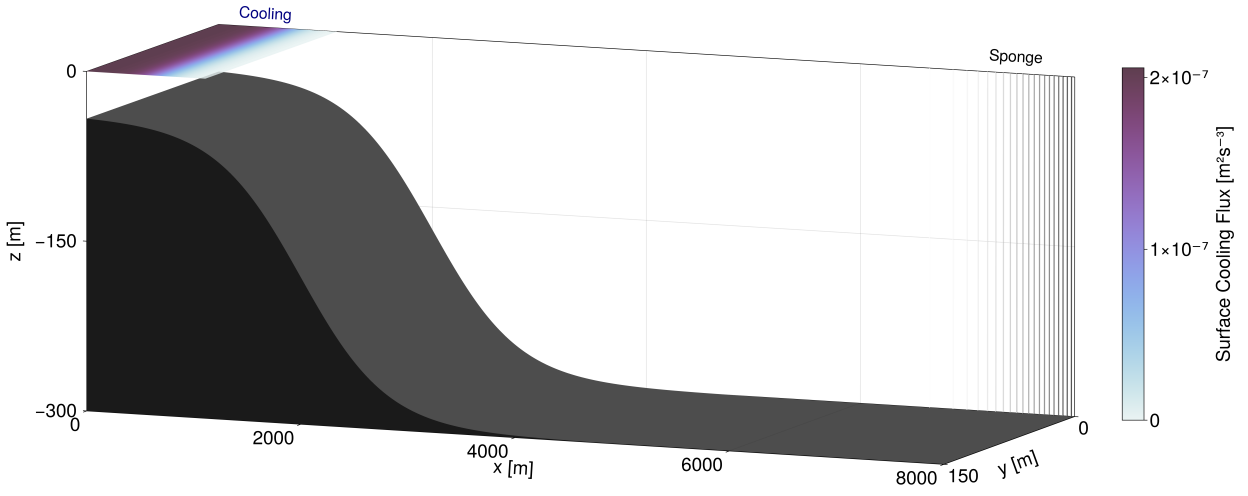



FIG. 1. Set up for 3D dense overflow LES. Gray contours show where the sponge region was applied to $u, w$ (across-slope and vertical velocities). Blue contours and colorbar indicate the shelf region cooling from the surface boundary condition on the buoyancy.

## 2. Numerical Set Up

To explore the dynamics of dense overflows, we used high-resolution LES, with a cooling surface boundary condition to develop a dense water overflow along sloping topography. The non-hydrostatic model in the Julia package Oceananigans (Wagner et al. 2025) was used to solve the incompressible Navier-Stokes equations under the Boussinesq approximation. A ninth-order weighted essentially non-oscillatory (WENO) scheme advects velocities and tracers, with a third-order Runge–Kutta time-stepping method. Poisson's equation for the non-hydrostatic pressure is solved using a conjugate gradient iterative solver, with a fast Fourier-transform based solver as a preconditioner (Wagner et al. 2025). We employed the explicit Smagorinsky–Lilly subgrid-scale model for the LES turbulence closure, with a turbulent Prandtl number of 1.

The domain, shown in Fig. 1, is three-dimensional, with size $(L_x, L_y, L_z) = (8000, 150, 300)$ m, with periodicity in the alongshore ($y$) direction and uniform grid spacing of $\Delta x = \Delta y = 4$ m and $\Delta z = 2$ m. A two-dimensional simulation with $(L_x, L_z) = (8000, 300)$ m is also used for the PV analysis in section 4. A 1500 m sponge-layer was applied on the offshore edge in $x$, damping $u, w$ velocities back to 0 to avoid wave reflection (gray contours, Fig. 1). Topography was included in the simulation using a grid-fitted immersed boundary method (Whitley Clark 2026). The topographic

slope is given by a tanh function, uniform in the alongshore direction, with depths ranging from 40 m on the shelf to the domain height of 300 m. Boundary conditions in the bottom normal direction were no flux on buoyancy and tracers and quadratic drag on momentum.

The domain is considerably smaller than a natural dense overflow, which forms plumes a few hundred meters thick that cascade downslope over distances of up to a few hundred kilometers (Magaldi and Haine 2015; Almansi et al. 2017; Colombo et al. 2020). Realistic simulations spanning such regions are correspondingly coarse, with horizontal resolutions generally of order 2 km or coarser (Magaldi and Haine 2015; Almansi et al. 2017). The reduced extent here relies on an assumption of dynamical similarity for high-Reynolds number flow, a deliberate trade-off for resolution: the boundary-layer PV fluxes and the NIW and SI interactions they set up require grid spacing of a few meters, which is computationally prohibitive over a full-scale overflow and rarely achieved in the large-scale models where such processes go unrepresented (Yankovsky and Legg 2019; Le Bras et al. 2022). The alongshore extent is kept narrow because the dynamics examined here are largely two-dimensional in the across-slope and vertical plane (section 4). This width falls below the baroclinic deformation radius, however, and so suppresses baroclinic eddies, whose potential role is addressed in the discussion.

The model is initialized at rest with a uniform stratification of $N_0^2 = 4 \times 10^{-7}$ s$^{-2}$ and a constant Coriolis frequency, $f = 1.43 \times 10^{-4}$ s$^{-1}$, chosen to match values found in the Denmark Strait, as well as previous simulations (Yankovsky and Legg 2019). Stronger stratification was tested ($N_0^2 = 4 \times 10^{-6}$ s$^{-2}$) and found to give qualitatively similar results, but the resulting overflows could not propagate into the deepest part of the domain, making the former case more amenable for further analysis. A cooling flux was applied to the buoyancy as a surface boundary condition over the shelf (blue surface shading in Fig. 1), extending approximately 400 m before decaying over the next 300 m, tapering off in the interior, preserving the length scale ratios and decay structure found in the larger scale simulations of Yankovsky and Legg (2019). This negative buoyancy forcing is set to approximately $2.057 \times 10^{-7}$ m$^2$s$^{-3}$, or equivalently a heat flux of 500 Wm$^{-2}$, consistent with the forcing magnitude used in Yankovsky and Legg (2019). A smaller heat flux of 50 Wm$^{-2}$ was also simulated, reproducing the same dynamics, but the larger length scales of the resulting overflow with the 500 Wm$^{-2}$ case make explanations and visualization clearer. The buoyancy forcing is temporally constant for 40 inertial periods, $T_f$, then is tapered off over 5 inertial periods,

allowing the system to reach quasi-equilibrium. The simulation is run for a total of $80T_f$, with a variable time step between $10^{-4}$ and 30 s, as determined by a CFL criterion of 0.5 within the simulation. An inertial period is approximately 12.2 hours, indicating a total simulation time of about 40 days. Diagnostics were calculated every 2400 s, except for the PV analysis (section 4), which required 60 s resolution.

## 3. Behavior of dense-water overflows in simulations

The following discussion of the general characteristics during the simulation will be split into two stages: active surface cooling from the shelf (overflow stage, $0-40T_f$) and after cooling is shut down (adjustment stage, $40-80T_f$). The overflow stage is mainly characterized by dense water formation (Dickson and Brown 1994; Girton and Sanford 2003; Magaldi et al. 2011). Once surface cooling is shut off, the resulting geostrophic adjustment and development of a deep boundary current serve as an idealized representation of the dynamics associated with surface buoyancy flux variability or the downstream response to an upstream cooling event (Köhl et al. 2007; Koszalka et al. 2013; Saberi et al. 2020; Chafik et al. 2023). In the latter view, the adjustment stage follows a segment of the boundary current as it leaves its formation region and flows along the slope, with time standing in for distance downstream.

### *a. Dense water formation and overflow*

The simulation starts from rest, but surface cooling quickly generates convection on the shelf. The dense water then begins to move down the slope due to a horizontal pressure gradient arising from the density contrast across the slope, but is deflected to the right ($v < 0$) by Coriolis, undergoing geostrophic adjustment. This results in a bottom geostrophic jet ($v < 0$), coupled with a return flow and an opposite-signed surface jet above ($v > 0$) (Fig. 2b). The along-slope velocity is an order of magnitude larger than $u$ (Fig. 2a), consistent with the flow being nearly geostrophic, though friction in the bottom boundary layer (BBL) induces a small ageostrophic component allowing the current to continue down the slope (Cenedese et al. 2004). The dense overflow results in isopycnals that roughly parallel the topography within the first 10 inertial periods (Fig. 2c). Animations of these fields over both stages of the simulation are provided in the supplementary material and give a fuller picture of the evolution described below.

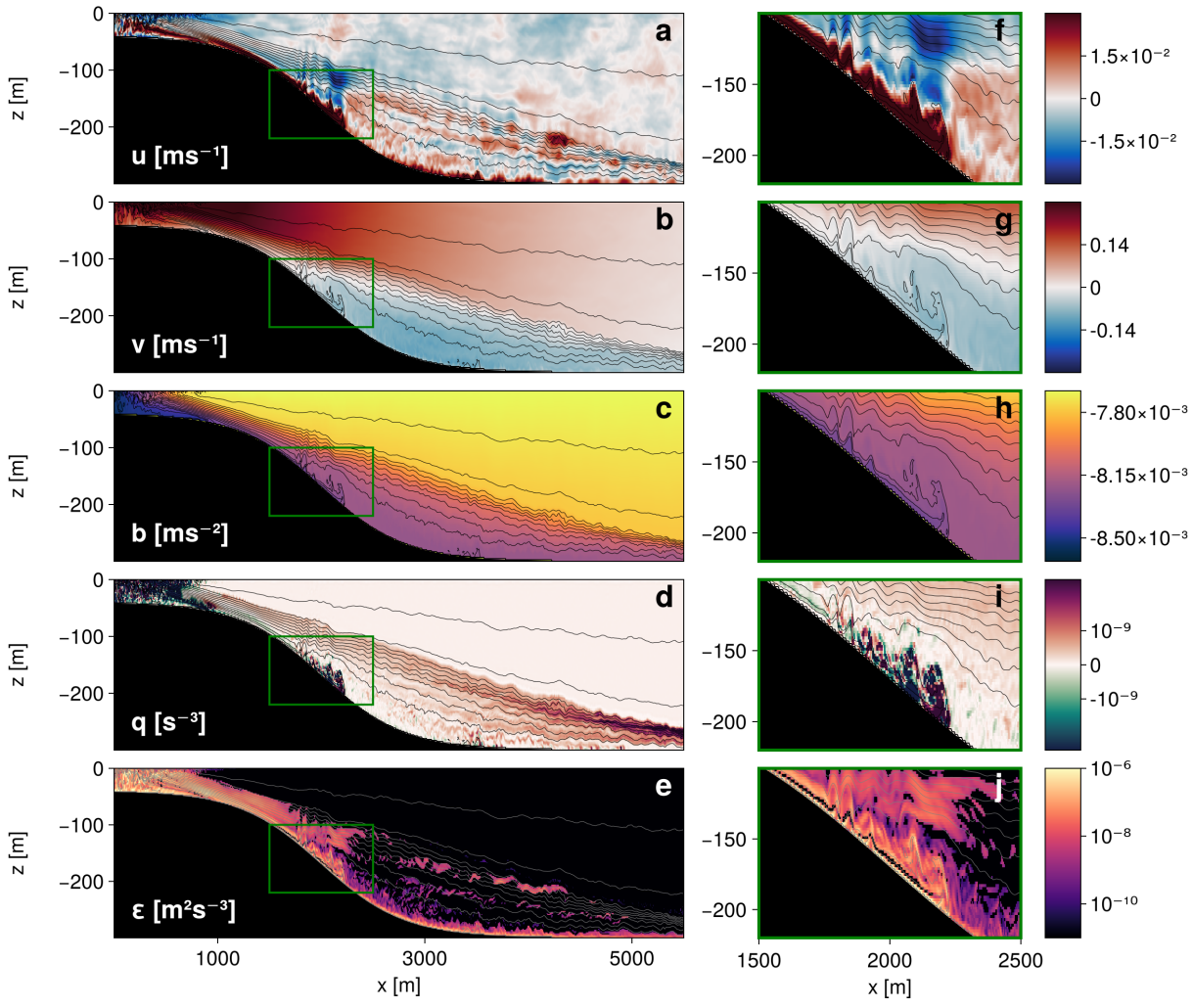



FIG. 2. Snapshots during the cooling phase at $t = 30.5T_f$ of the 3D simulation at $y = 74$ m. Fields shown are the across (a,f) and along-slope (b,g) velocities, $u, v$, (c,h) buoyancy, (d,i) the Ertel PV, and (e,j) in log scale, the dissipation rate of kinetic energy. Contour lines on all plots are isopycnals in units of buoyancy at intervals of $5\times10^{-5}$ ms$^{-2}$. (f-j) is a close-up of the green box in (a-e), showing a dense pulse carrying positive PV down the slope.

Strong vertical shear results in dissipation rates of kinetic energy on the order of $10^{-6}$ m$^2$s$^{-3}$ along the gravity current (Fig. 2e,j). The dissipation rate, $\epsilon$, is calculated directly from model fields as,

$$\epsilon = \nu_e \frac{\partial u_i}{\partial x_j}\frac{\partial u_i}{\partial x_j}, \tag{1}$$

where $\nu_e$ is the turbulent eddy viscosity, and summation over repeated indices is implied. The overflow also generates a robust internal wave field in the interior, along with banded structures in the across-slope velocity within the stratified bottom region along the slope ($x$ = 3000 – 5000 m, Fig. 2a). While dissipation is much stronger within the dense current, bands of elevated rates of dissipation of kinetic energy on the order of $10^{-8}$ m$^2$s$^{-3}$ are also found in this stratified interior (Fig. 2e).

During this formation stage, shelf cooling modulates the downslope flow by producing periodic, subinertial pulses of newly formed gravity currents, each exporting a successively denser buoyancy class (Fig. 2 f–j; see also the supplementary animations). Strong surface cooling and the relatively shallow domain allow each gravity current to fill the deepest part of the domain with new dense water (green contour, Fig. 3). Although similar subinertial overflow variability has been linked to upstream forcing or mesoscale processes (Girton and Sanford 2003; von Appen et al. 2014; Almansi et al. 2017) or to topographic Rossby waves propagating along the slope (Geyer et al. 2006; Darelius et al. 2011), these mechanisms are absent in the present idealized configuration. The periodicity is therefore tied to the cooling-driven evolution of the shelf buoyancy field, likely through cycles of convective densification and release.

Each gravity current begins with low PV due to the surface buoyancy loss, but gains PV as it travels down the slope (Figs. 2i, 3g). Ertel PV, $q$, is calculated as,

$$q = (\boldsymbol{f} + \boldsymbol{\omega}) \cdot \nabla b, \tag{2}$$

where $\boldsymbol{f}$ is the Coriolis vector, $\boldsymbol{\omega}$ is the relative vorticity vector, and $b$ is buoyancy. The overflow then advects this PV signature into the deepest part of the domain. The periodic passage of these currents and associated injection events produces a layered history of high PV that effectively "caps" the dense overflow near the base of the slope ($x \approx 5000$ m; Fig. 3(f-j)). Yankovsky and Legg (2019) reported thin bands of negative PV between high-PV layers, indicative of SI. Here, PV between high-PV bands instead remains low but positive. This suggests that NIWs, rather than SI, may be responsible for the banded velocity structures in the stratified interior noted above (Fig. 2a), whose propagation and associated mixing are examined in Part II (Whitley et al. 2026).

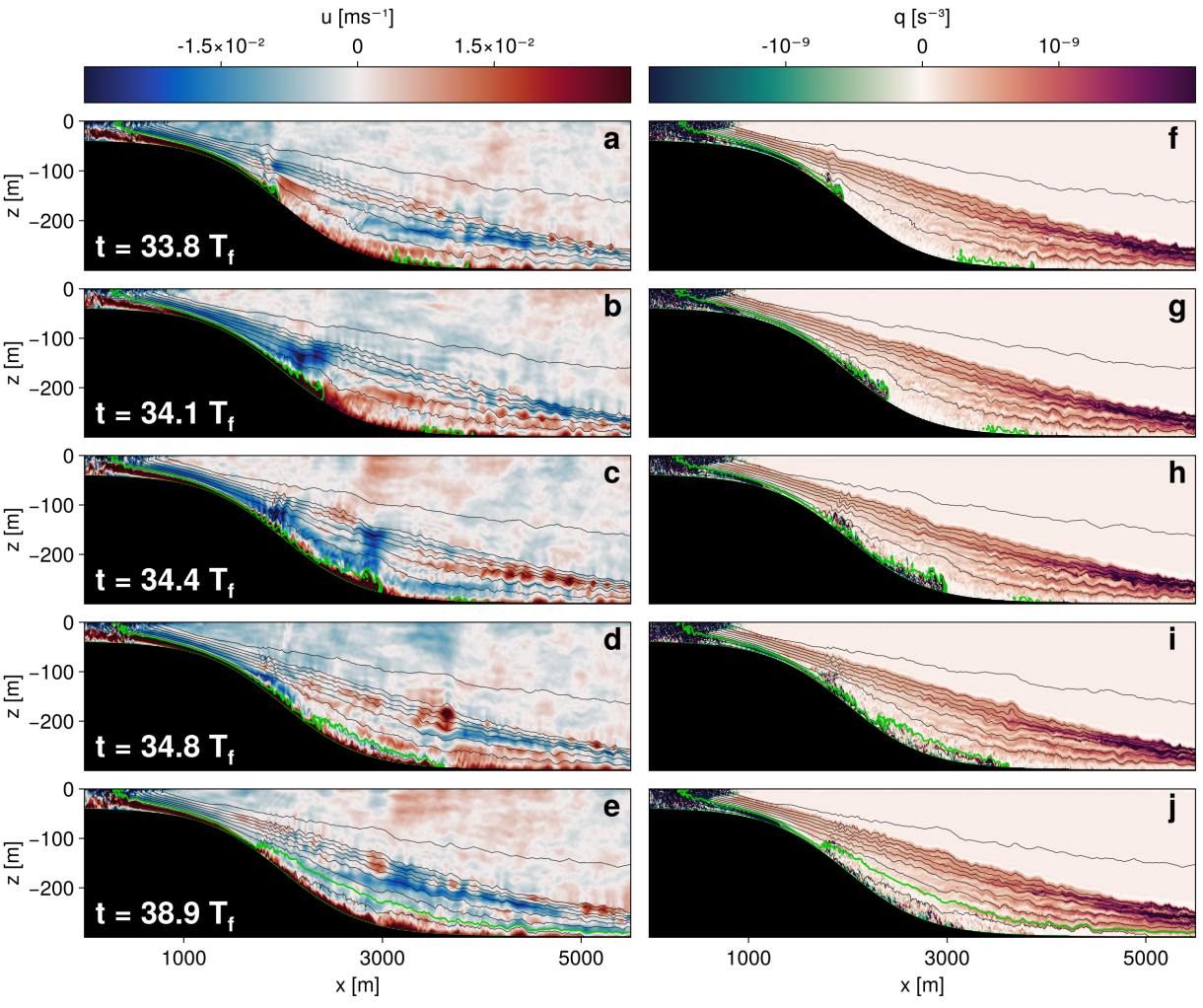



FIG. 3. Snapshots of the across-slope velocity, $u$, (a-e) and the Ertel PV, $q$, (f-j) during the passage of a representative gravity current in the 3D simulation at $y = 74$ m. Thin black contours in all panels denote isopycnals corresponding to evenly spaced buoyancy classes at intervals of $7.4 \times 10^{-5}$ ms$^{-2}$, while the thicker green contour highlights a specific buoyancy class marking the downslope progression of the gravity current and the subsequent convergence of high PV within the newly formed interior stratified layer.

### *b. Adjustment after the shutdown of cooling*

After the surface cooling is shut down, the gravity current largely stops, and the system further adjusts into geostrophic balance with the strongest buoyancy gradients near the shelf-break front (Fig. 4b,c). In this second stage, the isopycnals are approximately aligned with the slope,

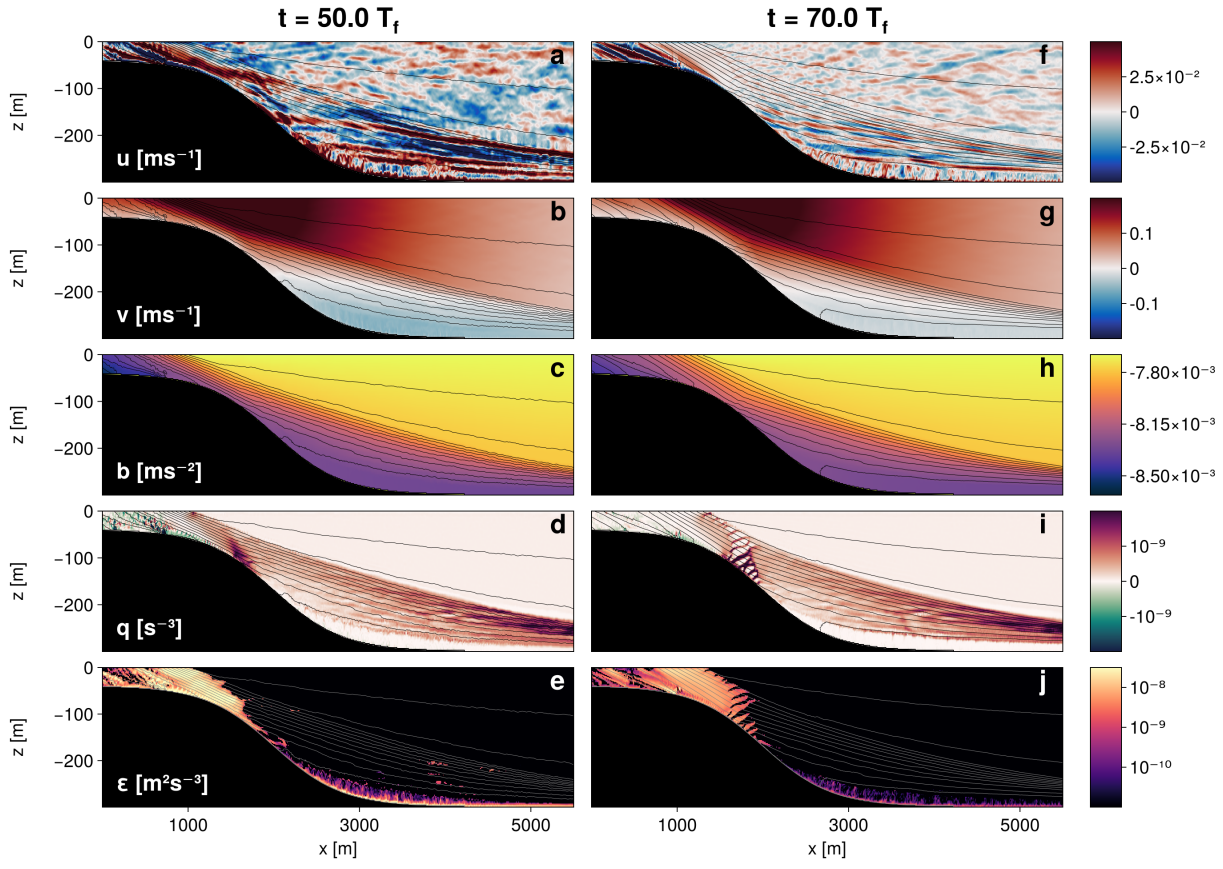



FIG. 4. Snapshots at $t = 50T_f$ (a-e) and $70T_f$ (f-j) of the 3D simulation at $y = 74$ m, after cooling has been shut off. Fields shown are the across (a,f) and along-slope (b,g) velocities, $u, v$, (c,h) buoyancy, (d,i) the Ertel PV, and (e,j) in log scale, the dissipation rate of kinetic energy. Contour lines on all plots are isopycnals at intervals of $5 \times 10^{-5}$ ms$^{-2}$.

outcropping over the shelf ($x = 700 - 1000$ m, Fig. 4c). The associated along-slope velocity structure persists with a slow spin-down over the duration of the simulation (Fig. 4b).

In the interior stratified layer ($x = 3000 - 5000$ m), the banded structures in the across-slope velocity field become much clearer without the active overflow (Fig. 4a), a remnant of the internal wave field generated during cooling (Whitley et al. 2026). In the more weakly stratified upper interior, the classic cross pattern in the $u$ velocity field (Fig. 4f) is similarly indicative of internal waves. The layers of high PV generated by the gravity current also persist, but without continued advection of newly generated PV down the slope, no new layers form (Fig. 4d,i).

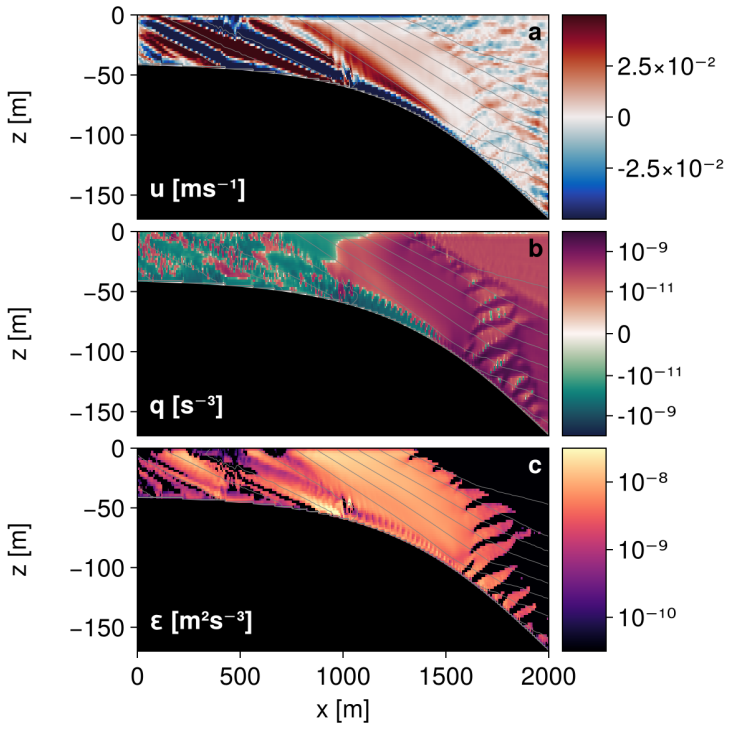



FIG. 5. The shelf region at $t = 70T_f$ of the 3D simulation at $y = 74$ m. (a) across-slope velocity, (b) Ertel PV, and (c) dissipation rate of kinetic energy. Both (b,c) are on a log scale. Contour lines on all plots are isopycnals at intervals of $5 \times 10^{-5}$ ms$^{-2}$.

Further up on the shelf ($x = 0 - 1000$ m), the PV is negative (Fig. 5b) and there are overturning cells aligned with isopycnals (Fig. 5a) consistent with SI. While there is no longer constant downslope flow, intermittent dense water pulses off the shelf every 3 – 5 inertial periods. One such pulse is visible near $x = 1000$ m in Fig. 5, associated with elevated dissipation at its head. Unlike the subinertial pulsing during the formation stage, these pulses of dense water find a resting buoyancy class partway down the slope ($x = 1500 - 2000$ m) and do not propagate further along the topography. The mechanism behind this intermittent shelf-water export will be discussed further in section 5.

Near the shelf break, a new feature of high PV appears shortly after cooling is shut down. Inspection of animations (see supplementary material) suggests the accumulation of the PV here is a result of weaker continuing export of shelf water which reaches its level of neutral density mid-way down the slope, along the topography ($x = 1500 - 2000$ m, Fig. 4d; see section 4). Over

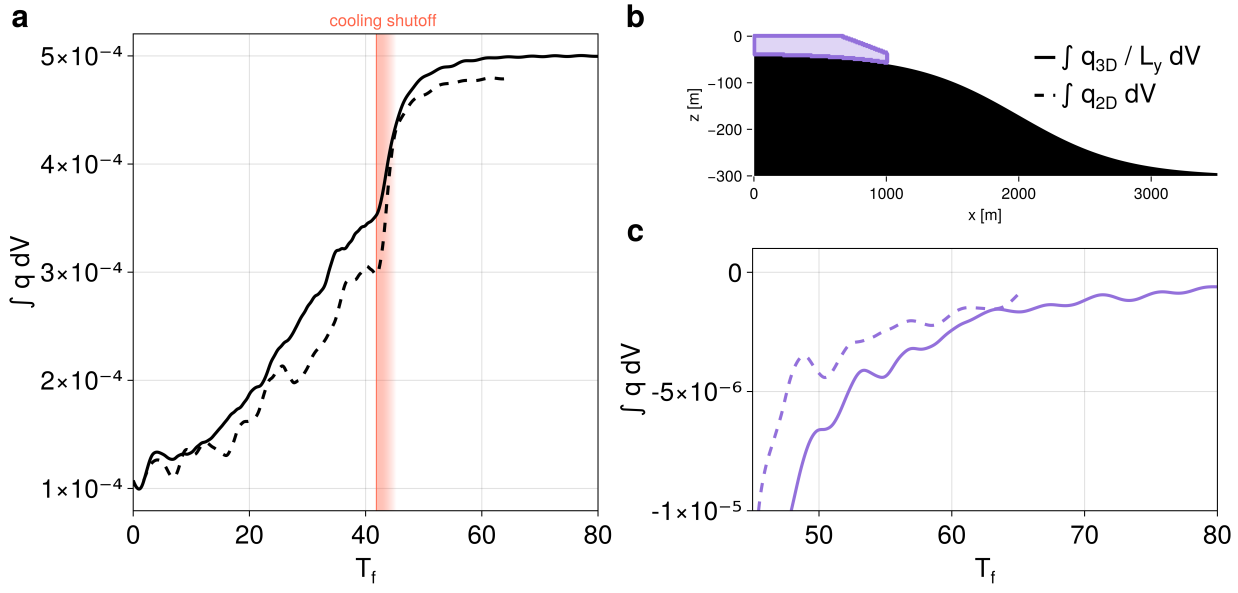



FIG. 6. Comparison between volume integrated PV from the 2D (dashed line) and 3D domain setups shows good agreement when 3D is normalized by the along-slope width ($L_y$) (solid line). (a) volume integrated PV in the full domain. (c) volume integrated PV on the shelf (region marked in purple in (b), cut to exclude the shelf break front) after cooling has been shut off. All terms have been smoothed by averaging over a rolling window of 1.75 $T_f$. Red shading in (a) marks the shutdown of the surface cooling with logarithmic shading of the cooling amplitude, ranging from 99% of full strength to $10^{-4}$.

time, this wedge of high PV organizes into tendrils of high stratification and high PV, intermixed with weak stratification and low PV (Fig. 5b). An accompanying wedge of elevated dissipation develops, with high dissipation concentrated in the low-PV regions between tendrils (Fig. 5c).

The surface cooling and subsequent dense overflow thus establish the conditions for both NIW interactions and submesoscale instabilities. The slope-aligned isopycnals and high-PV capping modify the propagation of incoming NIWs, examined in a companion paper (Whitley et al. 2026), while the negative PV generated on the shelf during cooling is favorable to SI (section 5). Although the remainder of the paper focuses primarily on the more quiescent adjustment stage, these features are inherited from the cooling stage and the overflow structures it leaves behind.

## 4. Potential vorticity in the dense-water overflow

The layered interior PV capping the dense overflow, the emergence of the high-PV wedge after cooling shuts down, and the persistence of negative PV on the shelf indicate a complex evolution of Ertel PV that differs from previously documented behavior (Yankovsky and Legg 2019). A detailed PV budget can identify the fluxes responsible and clarify how dense overflow dynamics and topographic interactions shape these PV features.

The Boussinesq governing equations on the $f$-plane for momentum and buoyancy are given by,

$$\frac{\partial \boldsymbol{u}}{\partial t} + \nabla \cdot (\boldsymbol{u}\boldsymbol{u}) + \boldsymbol{f} \times \boldsymbol{u} = -\frac{1}{\rho_0}\nabla p + b\hat{\boldsymbol{k}} + \boldsymbol{F} \tag{3}$$

$$\frac{\partial b}{\partial t} + \nabla \cdot (\boldsymbol{u} b) = \mathscr{D} \tag{4}$$

$$\nabla \cdot \boldsymbol{u} = 0 \tag{5}$$

where $\boldsymbol{u}$ is the velocity, $p$ is the pressure, $\rho_0$ is the reference density, and $\mathscr{D}, \boldsymbol{F}$ are the diffusion term and friction vector, respectively, which, for LES, include parametrized turbulent fluxes, as well as relevant boundary conditions. $\boldsymbol{f} = \langle 0, 0, f \rangle$ is the Coriolis vector. In this closed system, with no flow through the boundary, only boundary fluxes that alter the buoyancy or velocity can change the volume- (or isopycnal-) integrated PV (Haynes and McIntyre 1987). The sponge layer at the offshore edge damps only $u$ and $w$ and is uniform in $y$, so any PV flux is directed purely along $y$ and does not contribute to the volume-integrated budget in this system. Its influence on the flow and buoyancy near the offshore edge enters the budget only through the fluxes at that wall, which remain small. The PV boundary fluxes can be categorized as frictional (Fric) or diabatic (Diab), defined as

$$\text{Fric} \equiv -\boldsymbol{F} \times \nabla b, \tag{6}$$

$$\text{Diab} \equiv -\boldsymbol{\omega}_a \mathscr{D}, \tag{7}$$

where $\boldsymbol{\omega}_a$ is the absolute vorticity, $\boldsymbol{\omega} + \boldsymbol{f}$. The following discussion will focus on the important contributions from the PV fluxes through the top and bottom boundaries, in terms of Diab and Fric. A superscript will be used to denote the contribution of a given boundary to the volume-integrated PV tendency, rather than the flux vector itself; the contraction with the outward normal and its

accompanying sign are absorbed into the definition, so that a positive $\mathrm{Fric}^{\mathrm{top}}$ or $\mathrm{Fric}^{\mathrm{bot}}$ corresponds to a net PV increase within the volume from the top or bottom boundary (see Appendix for the full expansion). Since closing the budget requires output at a much higher temporal resolution than is feasible in 3D, the budget is evaluated in the two-dimensional $(x, z)$ configuration described in section 2, whose volume-integrated PV evolution closely tracks that of the 3D simulation (Fig. 6a); all fields are therefore assumed uniform in $y$ in what follows (see Appendix). Explicitly, $\mathrm{Fric}^{\mathrm{top}} = -\frac{\partial b}{\partial x} F^y\big|_{z=0}$, where $F^y$ is the along-slope component of $\boldsymbol{F}$, with equivalent expressions for Diab and for the corresponding contributions from the bottom boundary. Some results will also be discussed in terms of the total PV flux from a given boundary. For instance, the "top" PV flux is the net flux from the frictional and diabatic contributions along the surface: $\mathrm{Fric}^{\mathrm{top}} + \mathrm{Diab}^{\mathrm{top}}$. For a full description of the budget and its derivation and numerical implementation, see the Appendix.

### *a. PV evolution during dense water formation and overflow*

During cooling, the surface contribution is dominated by PV destruction over the shelf ($\mathrm{Diab}^{\mathrm{top}} < 0$, $x \lesssim 600$ m; Fig. 7a,c). This destruction arises from the change in buoyancy due to the surface cooling flux acting on the absolute vorticity. Here the lateral shear in the along-slope flow is comparable in magnitude to the planetary vorticity, and enhances the diabatic PV flux (Fig. 8e). Past the shelf break, surface fluxes are negligible ($x \gtrsim 1000$ m; Fig. 7a,c). Yet, despite these strong negative fluxes, the volume-integrated PV increases substantially during cooling (Fig. 6a).

Bottom boundary fluxes play a leading role in the net PV injection and consequent high PV structures in the stratified interior. The spatial structure of the bottom fluxes along the topography is complex (Fig. 7a). Below the cooling region, a frictional deceleration of the along-slope flow in the presence of a positive across-slope buoyancy gradient destroys PV. Upslope velocity indicative of upslope Ekman transport ($x < 700$ m, Fig. 8a) brings light water along the bottom into the denser shelf environment, destroying local PV. This PV destruction is contrary to the classic case of Ekman transport across a sloping bottom due to the shelf's positive horizontal buoyancy gradient (e.g. lighter water being found towards deeper water, c.f. Benthuysen and Thomas 2012).

Closer to the shelf break, the gravity current flows along the bottom ($x = 800 - 2000$ m, Fig. 8a), generating a strong positive frictional PV flux (Fig. 7a). Downslope flow now carries dense water along a steep bottom buoyancy gradient (Fig. 8f), injecting PV into the interior with each

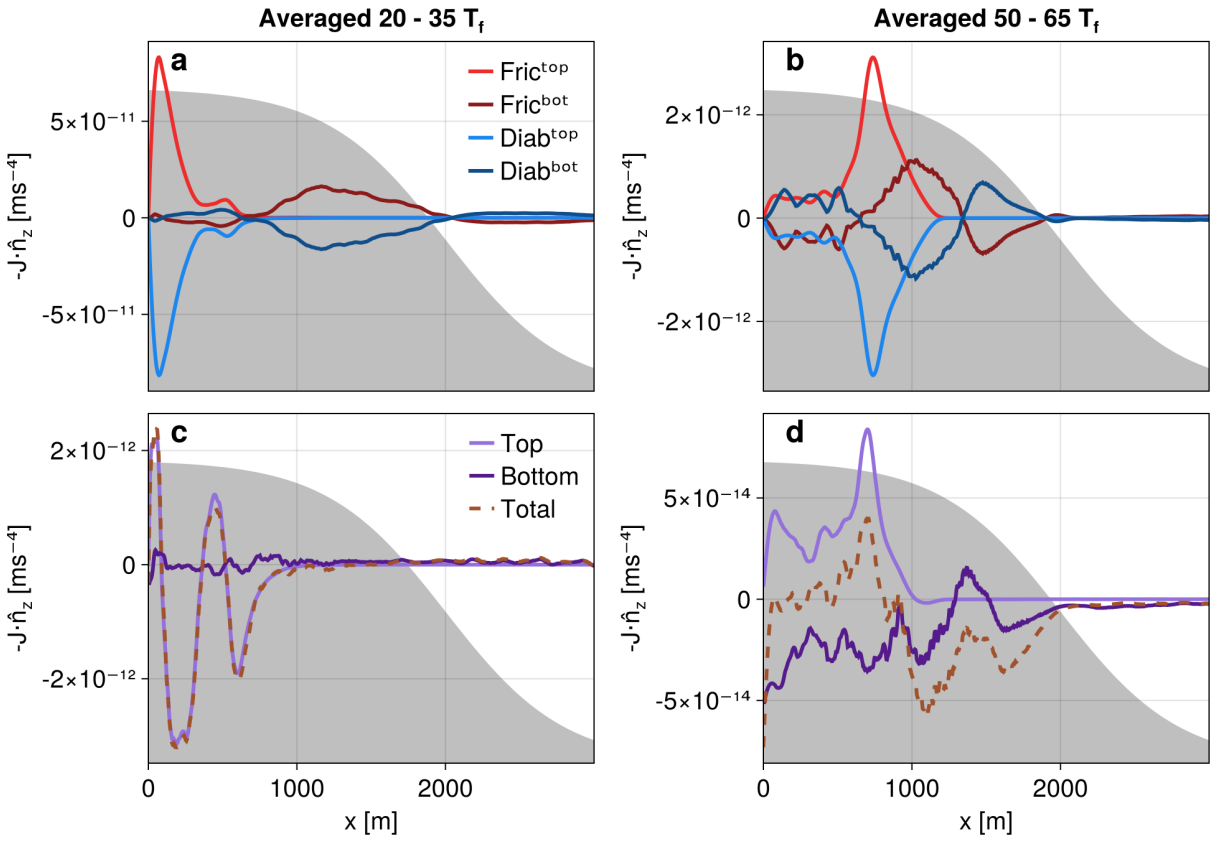



FIG. 7. Contribution to the vertical flux terms in the $x$ direction before integrating the budget (A6, see Appendix), averaged over equivalent amounts of time during the cooling period ($20 - 35T_f$, a,c) and after cooling has completely shut down ($50 - 65T_f$, b, d), highlighting the location along the slope where different vertical PV flux components dominate. (a,b) split the fluxes by both the location and physical component of the flux, while (c,d) show the net vertical flux along the top and bottom wall, as well as their combined contribution. Values are smoothed in $x$ by averaging over a rolling window of 40 m.

passing dense pulse. Hovmöller diagrams along the slope show these passing gravity currents, corresponding to a negative buoyancy anomaly and strong, positive horizontal velocity (Fig. 9 a,b). The PV along the bottom quickly changes from negative to positive at the shelf break, where the $Fric^{bot}$ flux is strongest (Fig. 9 c,d). As described in section 3a, it is this shelf break flux of high PV from $Fric^{bot}$ that is advected into the interior, creating the thin layers of high PV far from their generation site (Fig. 3).

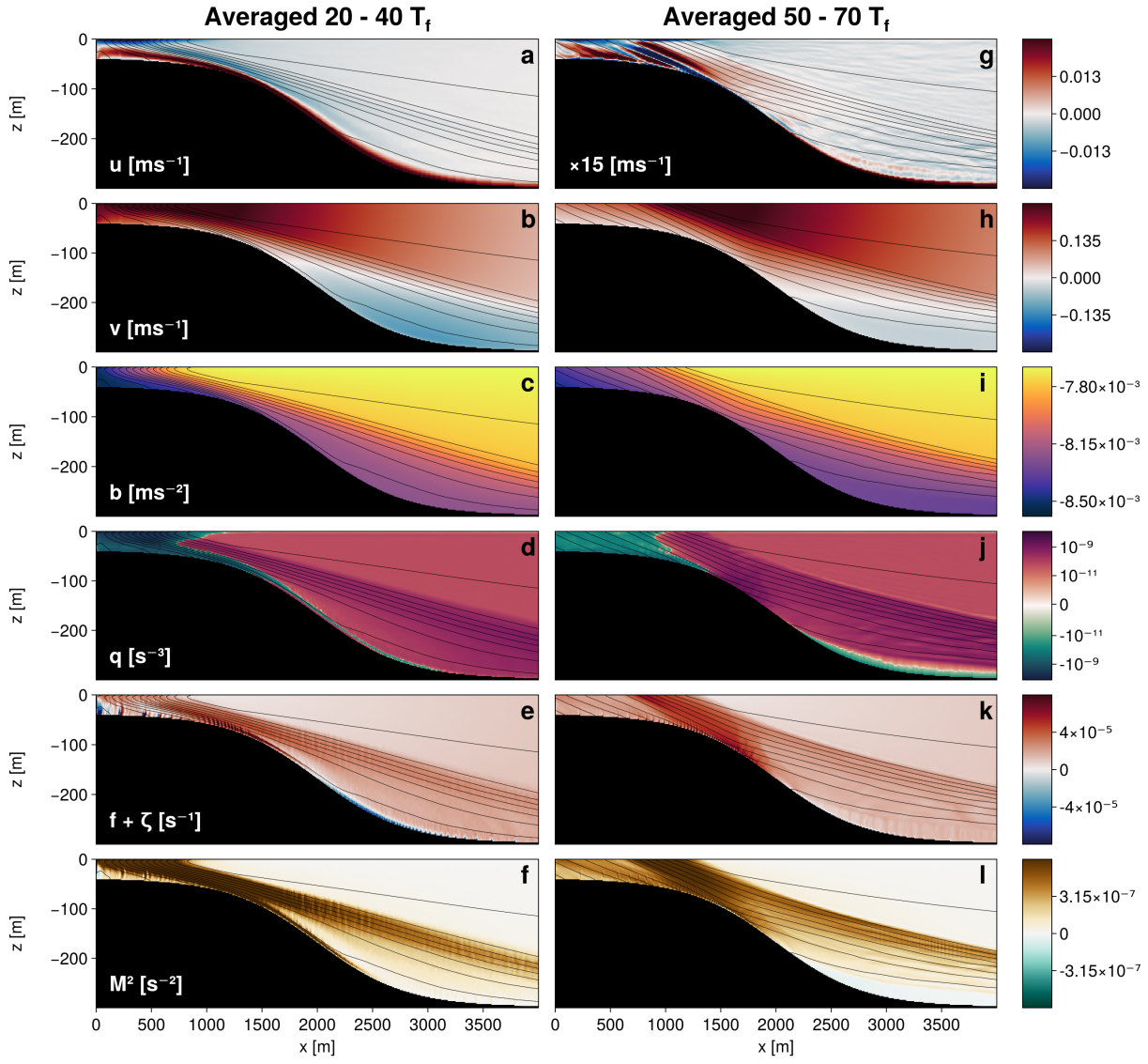



FIG. 8. Long-term averages over $20-40T_f$ (a-f) and $50-70T_f$ (g-l) from the 3D simulation. (a,g) across-slope velocity, $u$, where (g) is multiplied by 15 to be able to show both the dense overflow and the weaker magnitudes found after cooling is shut off, (b,h) along-slope velocity, $v$, (c,i) buoyancy, (d,j) PV, (e,k) absolute vertical vorticity, and (f,l) horizontal stratification, $M^2 = \partial b/\partial x$. Contour lines in all plots are isopycnals at intervals of $6.5\times10^{-5}$ ms$^{-2}$.

Further downslope, bottom fluxes change sign again ($x$ = 2000 – 3000 m, Fig. 7a). Here the deep along-slope flow ($v < 0$) drives downslope Ekman transport that carries dense water beneath lighter water (Fig. 8a,c). This is the classic destabilizing Ekman buoyancy flux, which frictionally

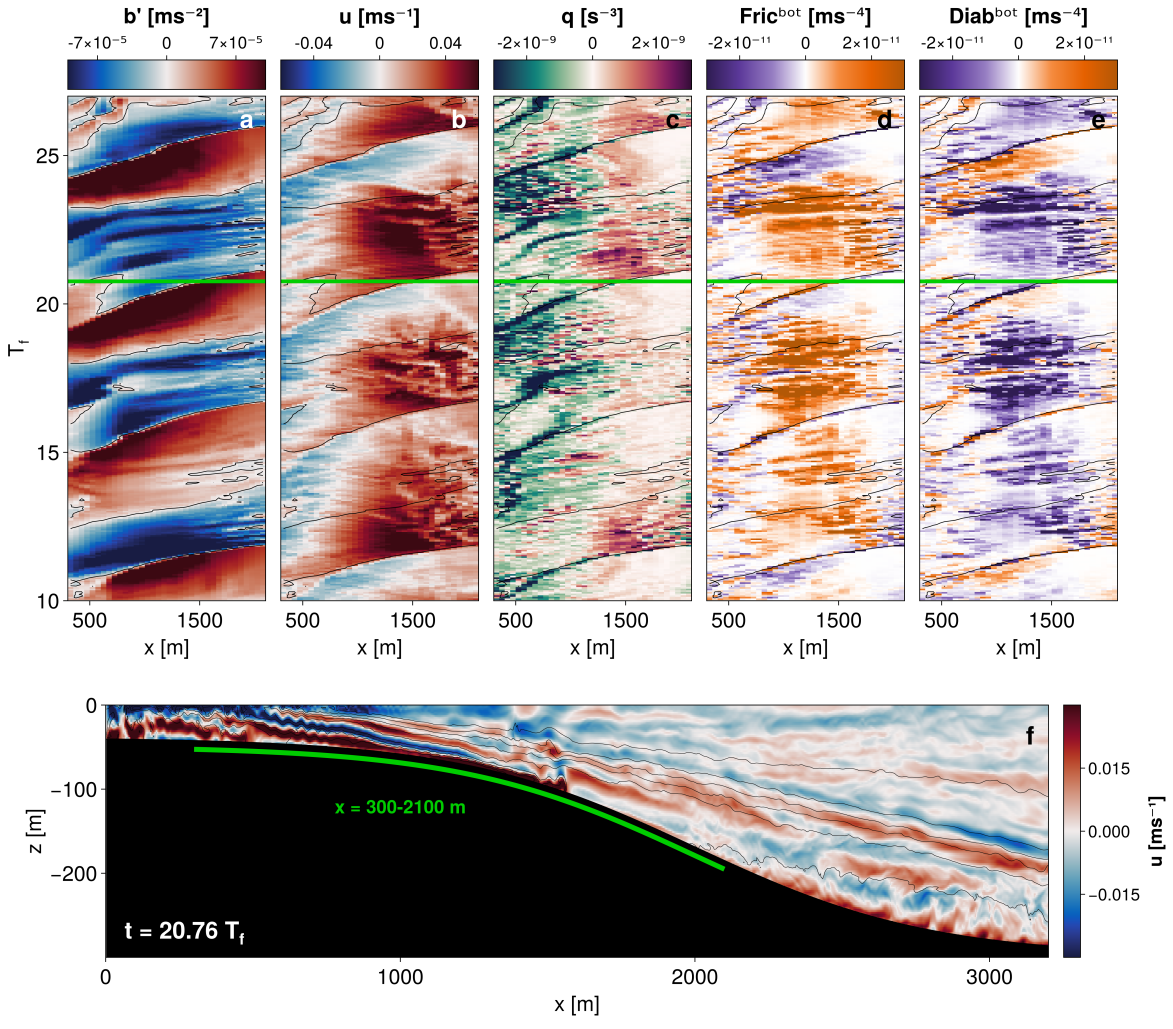



FIG. 9. Hovmöller plots, over 10–27 $T_f$, along the bottom boundary of (a) the high-pass ($7T_f$) filtered buoyancy anomaly, $b'$, (b) across-slope velocity, $u$, (c) PV, $q$, and the (d) frictional and (e) diabatic components of the bottom PV flux. Values are taken in the first cell above the topography and smoothed with a 100 m running average in $x$. Black contours mark the buoyancy anomaly, $b' = 0$, to denote the passing gravity currents in (a-e). The green horizontal line marks the time of the snapshot shown in (f): across-slope velocity at $t = 20.76T_f$ with buoyancy contours in black at intervals of $6.6\times10^{-5}$ ms$^{-2}$ and the corresponding stretch of slope used in (a)–(e) shown in green.

destroys PV at the boundary ($\text{Fric}^{\text{bot}} < 0$, Fig. 7a; Benthuysen and Thomas 2012; Wenegrat and Thomas 2020). The resulting thin boundary layer has negative absolute vorticity (Fig. 8e). As the dense current descends it is entraining warmer, ambient water ($\mathscr{D} > 0$). Therefore, with the

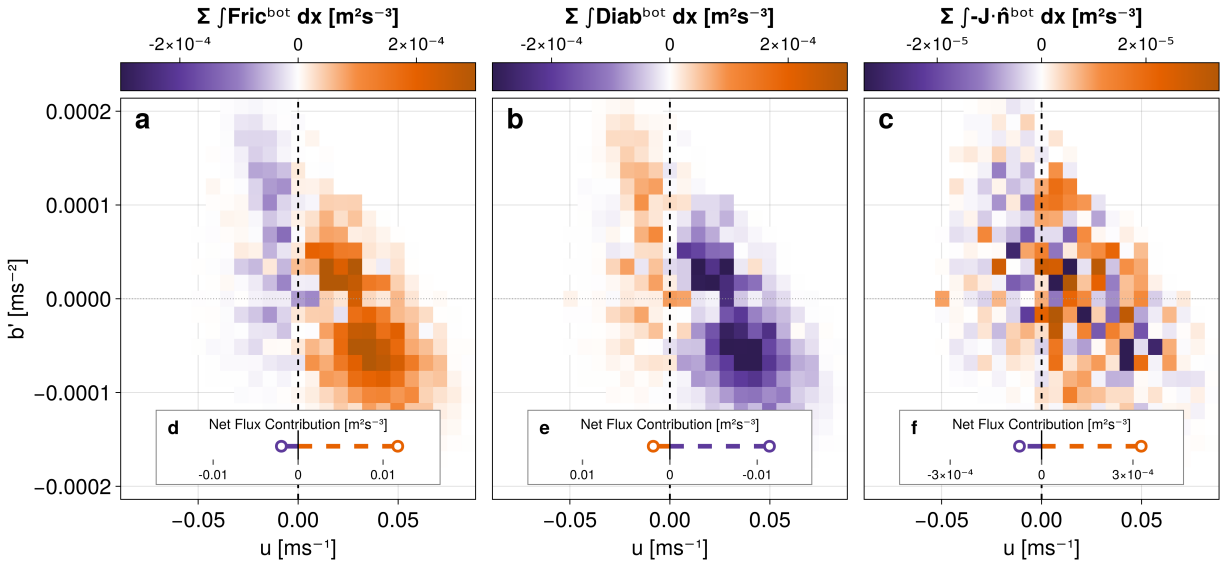



FIG. 10. Bottom PV flux binned in $u$–$b'$ space over $x$ = 0–4000 m over 10–40$T_f$, with (a) the frictional and (b) diabatic components, and (c) the total bottom flux. Each cell, with uniform bin size of $(\Delta b', \Delta u) = (1.711 \times 10^{-5}$ ms$^{-2}$, 0.0071ms$^{-1})$, is the net, time-integrated contribution summed over all $x$ and time. The black, dashed line marks $u = 0$. Insets (d)–(f) give the net contribution from either side of $u = 0$. Note flipped axis in (e).

absolute vorticity reversed this buoyancy tendency, which destroys PV at the shelf break, now produces a small, positive diabatic PV injection along the bottom boundary (Fig. 7a). However, both contributions are minor compared to the larger shelf-break frictional injection that the gravity current advects into the same region.

Binning the bottom PV fluxes during cooling along the full slope ($x < 4000$ m), based on the buoyancy anomaly and horizontal velocity at that time and location, shows the strongest fluxes coincide with the dense ($b' < 0$), downslope ($u > 0$) flow of the passing gravity currents (Fig. 10 a,b). While the corresponding total bottom PV flux histogram (Fig. 10c) is slightly less coherent than the individual frictional and diabatic components, the downslope phase of the gravity current shows a net-positive flux contribution (Fig. 10 f). This bottom injection largely controls the positive PV in the stratified interior ($x$ = 3000–5000 m, Figs. 3, 8d), as advected from the shelf break.

Overall this progression during cooling can be summarized as surface diabatic fluxes account for the negative PV on the shelf ($x < 1000$ m, Fig. 8d), while the passage of dense gravity currents

injects positive PV through a frictional flux along the bottom boundary. Although the bottom PV injection might appear weaker in magnitude than the surface cooling flux in a long-time average, it substantially counteracts surface PV destruction (Fig. 6a). Both the frictional bottom injection and surface diabatic fluxes play crucial roles in shaping the PV distribution within the dense overflow during the cooling stage, and ultimately the dynamics of the interior.

*b. PV evolution after the shutdown of the dense overflow*

After cooling ceases, frontal adjustment drives a frictional PV injection at the shelf-break front that dominates the PV budget (Figs. 6a, 7b,d). With surface buoyancy forcing removed, diabatic PV destruction drops sharply. The localized injection then drives a rapid increase in the volume-integrated PV ($40 - 45T_f$, Fig. 6a). As the gravity current weakens and the flow adjusts more towards geostrophic balance, vertical shear concentrates at the front where buoyancy gradients are strongest, producing the injection at the surface (Fig. 8g,h). This injected PV is advected to the level of neutral buoyancy where it accumulates, initiating the high-PV wedge at the shelf break (Fig. 8j, 5). PV flux magnitudes then decrease, and the flow enters a less turbulent phase with markedly weaker PV fluxes (Fig. 7b). The peak surface flux stays concentrated at the shelf-break front (Fig. 7b), where large buoyancy gradients sustain strong along-slope shear, intensifying surface velocities and relative vorticity (Fig. 8h,k).

The bottom PV flux retains three distinct regions along the topography, though all are weak. On the shelf, a mean upslope velocity combined with a positive along-slope flow (Fig. 8g,h) suggests on-slope Ekman transport (MacCready and Rhines 1991). Because shelf waters remain denser than the interior, the positive lateral buoyancy gradient (Fig. 8l) results in a negative $\text{Fric}^{\text{bot}}$ (Fig. 7b), as during the cooling phase in this region (Benthuysen and Thomas 2012). At the shelf break, the passage of the weaker post-cooling dense pulses results in negative $\text{Diab}^{\text{bot}}$ and transient PV destruction (Fig. 7b,d). Under the deep boundary current ($x > 2000$ m), downslope Ekman transport destroys PV (Fig. 7d), but this thin layer of negative PV is capped by the stronger high PV in the stratified layer (Fig. 8 j). While such a boundary layer can be unstable to SI in some configurations (Wenegrat and Thomas 2020), no evidence of SI is found in this layer here.

Although flux magnitudes drop after cooling ceases, the PV structures established during the cooling phase persist. The banded high-PV in the stratified interior, set up by bottom-boundary

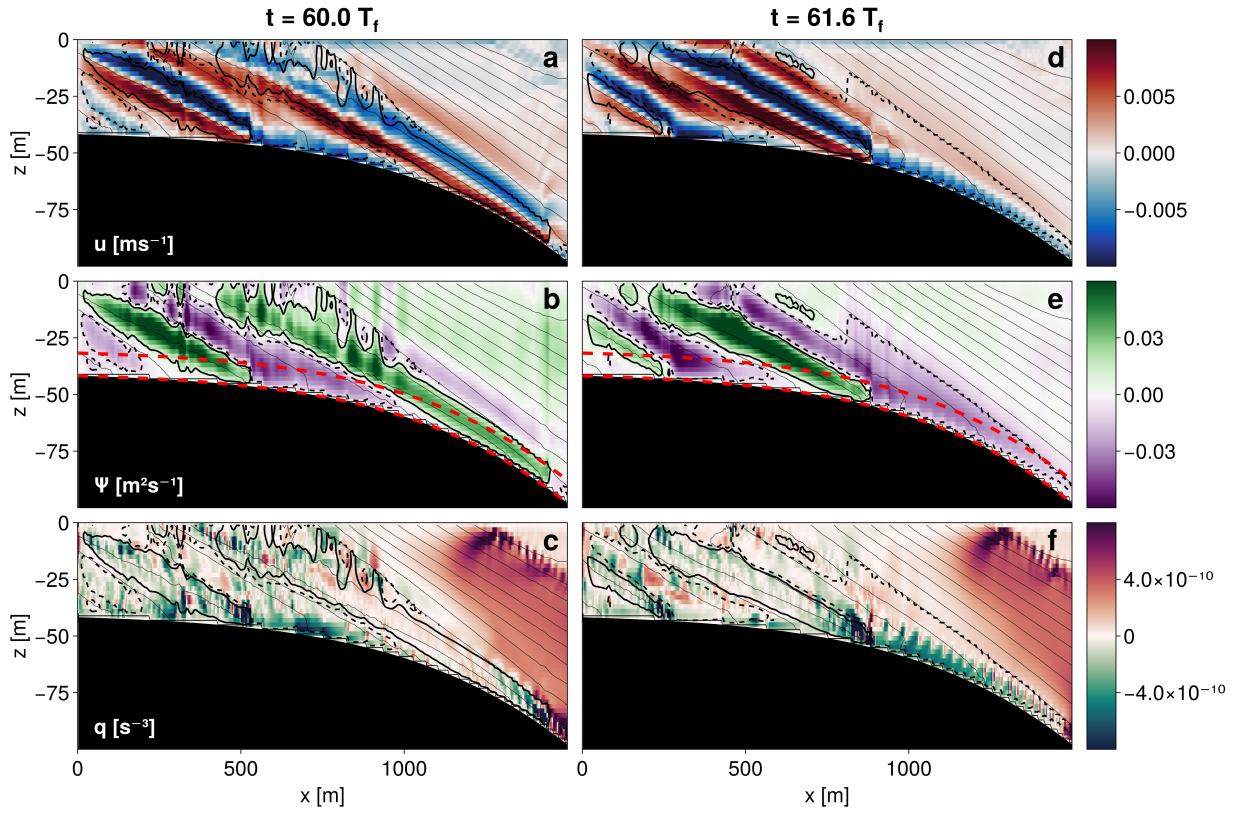



FIG. 11. Shelf region cross-sections of (a,d) $u$, (b,e) stream function for the flow, and (c,f) PV at two times, $t = 60T_f$ and $t = 61.6T_f$. Isopycnals at intervals of $4.3 \times 10^{-5}$ ms$^{-2}$ are superimposed as thin lines, while clockwise (counter-clockwise) stream function contours are marked with thick dashed (solid) lines. Green (purple) shading indicates counter-clockwise (clockwise) circulation, $\Psi > 0$ ($\Psi < 0$). Red dashed contour lines in (b,e) mark the region used in Fig. 12. The two snapshots show the across-slope propagation of the SI cells towards the shelf-break front, where the magnitude of the vertical shear is strongest.

injection from passing gravity currents, is maintained. The negative PV left on the shelf by the cooling itself also persists. Together with the creation of the high-PV wedge by the surface injection during frontal adjustment, these features create the PV structure that modifies the propagation of NIWs in the interior, examined in a companion paper (Whitley et al. 2026), and promotes SI on the shelf (Section 5).

## 5. Symmetric instability and shelf water export

While the stratified interior is entirely stable to SI ($x$ = 3000–6000 m, Fig. 8j), the negative PV generated on the shelf by surface cooling remains favorable to SI. Here, the shelf is defined as the first 1000 m, with a slanted offshore boundary to exclude the shelf-break front (Fig. 6b). After cooling shuts down, SI manifests as coherent slantwise overturning cells aligned with isopycnals (Haine and Marshall 1998). The overturning structure can be seen in the $u$ velocity and corresponding streamlines, $\Psi$, in Fig. 11, where green ($\Psi > 0$) indicates counterclockwise rotation.

While analysis of SI is often focused on the rapid PV adjustment toward marginal stability ($q \approx 0$, Thorpe and Rotuno 1989; Taylor and Ferrari 2009; Chor et al. 2022), here the primary dynamical signature is the organized, propagating structure of the SI cells themselves, which drive lateral transport on the shelf. The reduction of PV toward marginal stability tends to occur on inertial timescales (Thorpe and Rotuno 1989; Taylor and Ferrari 2009; Chor et al. 2022), but is comparatively slow in the present configuration. Continuous bottom PV destruction, likely associated with upslope Ekman transport (see section 4, and Whitley Clark 2026), offsets the stabilizing effect of SI. As a result, negative PV persists on the shelf for the full duration of these simulations. Here, however, we focus the analysis on a 10-inertial-period window ($50 - 60 T_f$) after the surface cooling has fully shut down, as it is expected that three-dimensional effects (including baroclinic instability) in realistic settings will modify the evolution over longer timescales.

The SI cells here propagate subinertially offshore, in contrast to the stationary structures often seen in idealized surface-front configurations. For example, the leading counterclockwise cell initially spanning $x$ = 0–500 m in Fig. 11b (marked in green) advances approximately 250 m over $1.6 T_f$ (Fig. 11e; the propagation is most easily seen in the supplementary animations), corresponding to a propagation speed of $\sim 0.4$ cm s$^{-1}$. Pedlosky (2014) showed that SI cells translate when the basic state varies slowly across the shelf ($x$). An across-shelf variation of the along-shelf vertical shear ($\partial v / \partial z$) drives SI cells toward regions of stronger shear, while a variation of depth alone moves them toward shallower water. In previous simulations of the Oregon continental shelf and other idealized models, SI cells were found to translate across the slope in the onshore direction (Allen and Newberger 1996; Brink and Cherian 2013). Here the cells translate offshore, into deeper water and toward the stronger shear at the shelf-break front, consistent with the shear variation and opposite to the direction expected from the depth variation. A test with a

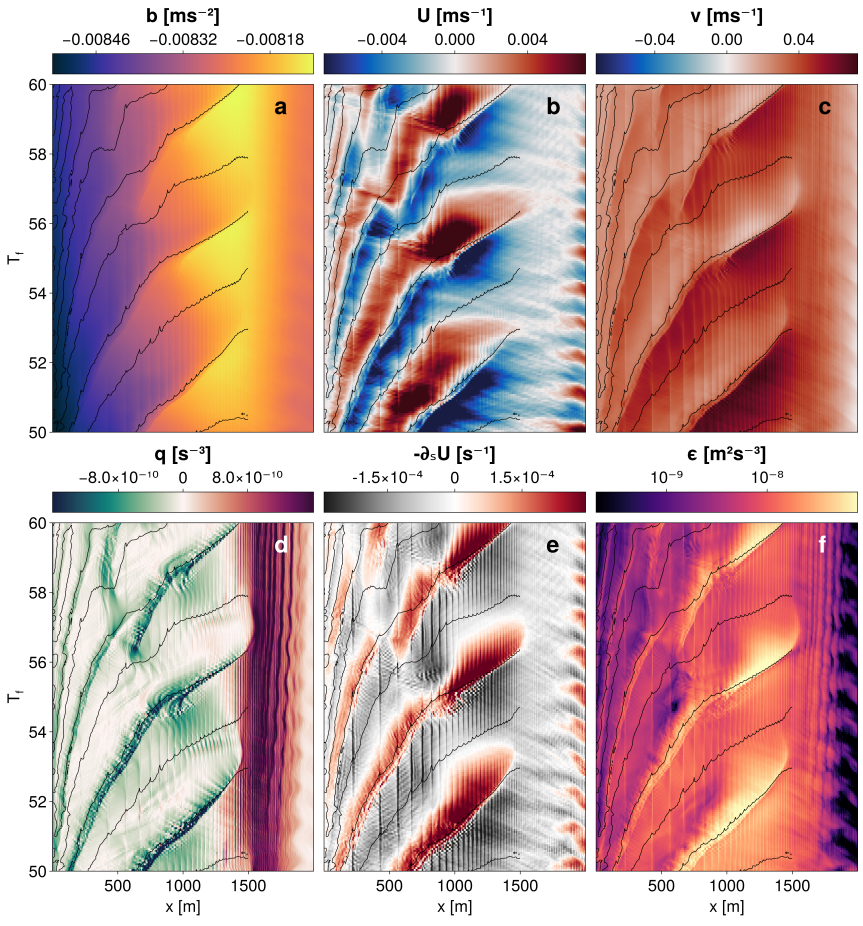



FIG. 12. Hovmöller plots of (a) buoyancy,(b) across-slope velocity tangential to the sloping bottom, $U$, (c) along-slope velocity, $v$, (d) PV, (e) convergence of the bottom-tangential velocity, $-\partial_s U$, where $s$ is the across-slope coordinate measured along the bottom, and (f) the dissipation rate of kinetic energy, $\epsilon$, along the shelf averaged over the bottom 10 m, as marked by red dashed lines in Fig. 11b,e, for 10 inertial periods ($50 - 60 T_f$) after cooling is completely shut down. Black contours mark the high-pass filtered buoyancy anomaly, $b' = 0$, to denote the passing pulses, stopped before the shelf-break front at $x = 1500$ m.

completely flat shelf region still produces cells propagating toward the strong vertical shear (not shown here), confirming that the across-shelf variation of the shear, rather than the topography, drives the offshore translation of the SI cells here.

Convergent regions between adjacent SI overturning cells organize dense anomalies into coherent pulses that travel along the shelf. Hovmöller diagrams of the vertical average of the near boundary region (below red, dashed line in Fig. 11b,e) show the propagation of these features along the shelf

(Fig. 12). Since the averaging region lies within 10 m of the sloping topography, the velocity in the $x$–$z$ plane is decomposed into components tangential and normal to the local bottom by rotating $(u, w)$ through the local bottom-slope angle. $U$ denotes the tangential across-slope component, positive offshore, and $s$ the across-slope coordinate measured along the bottom. Convergent regions, identified by ($-\partial_s U$, Fig. 12e), progress toward the shelf break, carrying dense water offshore along the bottom boundary (Fig. 12a,b). The zero contour of the buoyancy anomaly denoting the edges of these pulses is also marked in Fig. 12, as defined with a high-pass Gaussian filter removing trends longer than 6 $T_f$. These pulses recur every 3–5 inertial periods and are associated with strong dissipation and pronounced PV anomalies (Fig. 12d,f). Note that the growth of the high-PV wedge after the shelf break can also be seen between $x$ = 1500 – 2000 m (Fig. 12d,f).

The offshore propagation of SI cells and their associated dense pulses generate cross-shelf transport. The pulses initially move at the cell propagation speed, but as they approach the shelf break, the increasing topographic slope causes them to detach from the parent SI cells and descend beyond the region where the cells are located on the shelf (e.g., see the pulse near $x$ = 1500 m, Fig. 11a-c). This transition is accompanied by an acceleration in the downslope direction ($x$ = 1000 – 1500 m, Fig. 12b), likely due to its evolution into a gravity current. These pulses descend until reaching a neutral buoyancy level near $x$ = 1500 m.

This process leads to periodic, SI-driven export at the shelf break, as shown in buoyancy space in Fig. 13. Off-shelf export is defined as the total transport within each buoyancy class at the "shelf break," defined as $x$ = 1000 m (as marked in Fig. 13c). Propagation of the SI cells delivers pulses of dense water to the shelf break, producing episodic export events visible in the densest buoyancy classes in Fig. 13b. The total transport from each buoyancy class during the time period between 50 and 60$T_f$ is plotted in Fig. 13a, highlighting the net export from the densest buoyancy classes. For more physical intuition, this quantity has also been plotted on the buoyancy field averaged over the same time period in Fig. 13c. The dense pulse export is from the lighter red regions, mostly located before the shelf break in Fig. 13c, below $b = -0.0082$ ms$^{-2}$ in Fig. 13a. While buoyancy classes along the left edge of the shelf-break front experience strong bidirectional exchange, these competing fluxes largely cancel in net. As a result, the integrated export is dominated by dense water coming from the shelf, with total dense export nearly three times larger than the intermediate

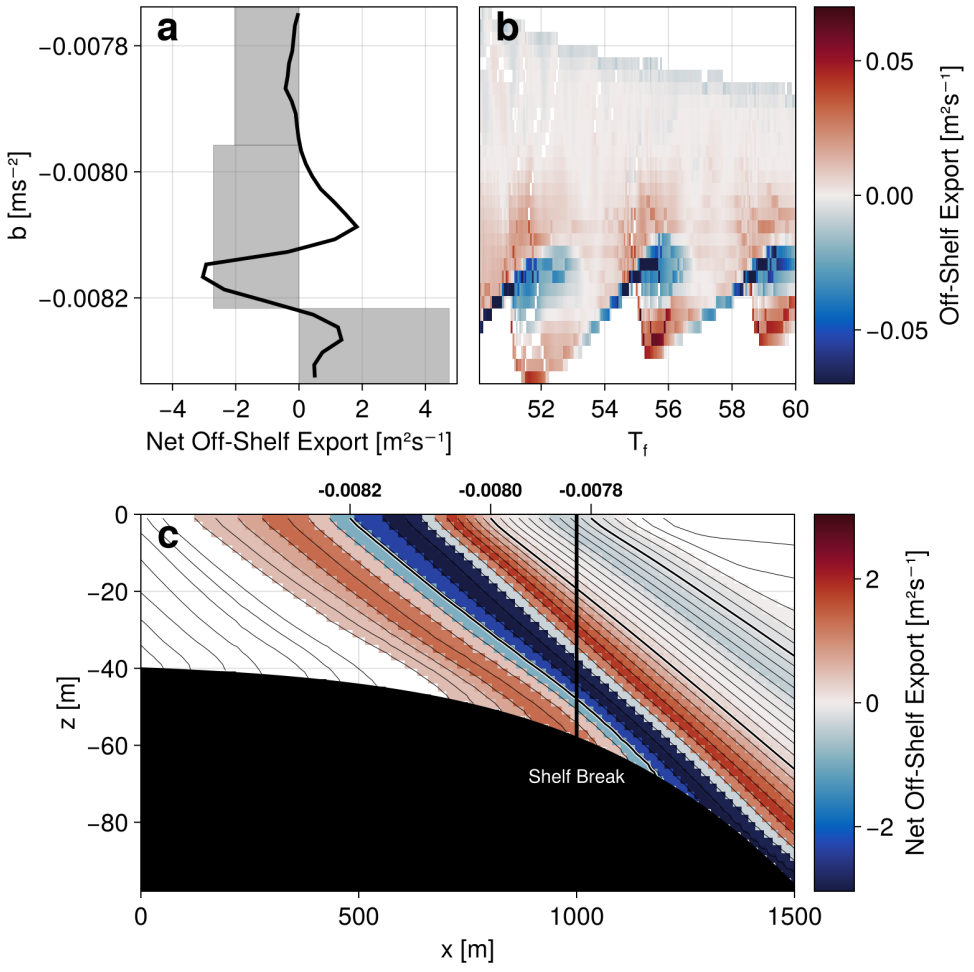



FIG. 13. Net export off shelf in buoyancy space as defined by the vertical cross section at $x = 1000$ m, shown by the labeled black line in c. (a) the sum over time, for 10 inertial periods $(50-60T_f)$ after cooling is completely shut down, of the transport across the shelf break, binned in 30 buoyancy bins. The gray bars show the net transport over the buoyancy classes spanned, showing that the export by the densest shelf buoyancy classes is larger than the import/export at the shelf break. (b) buoyancy-binned transport in time, before the sum is taken. (c) net export plotted from (a) in the corresponding buoyancy bin in physical space, using the buoyancy averaged over the same time period as (a,b). Contours are taken at bin sizes of $2\times10^{-5}$ ms$^{-2}$, with the three labeled contours in (c) corresponding to the axis labels in (a). Positive values in all plots indicate off-shelf export.

buoyancy class import (see gray bars in Fig. 13a for the net export from upper, intermediate, and lower buoyancy classes).

These results identify a subinertial, SI-mediated pathway for cross-shelf export. After surface cooling ceases, the shelf remains dynamically active due to SI which organizes into slantwise overturning cells that propagate offshore across the shelf. Convergent regions between adjacent cells assemble dense, low PV anomalies into coherent pulses, which are carried toward the shelf break with the propagating cells. On reaching the steepening topography, the pulses detach from the parent cells and descend the slope to a neutral buoyancy level. SI-driven transport thus adds to the known mechanisms of subinertial cross-shelf export (e.g., Huthnance 1995; Gawarkiewicz and Chapman 1995; Shapiro and Hill 1997; Ivanov et al. 2004; Lentz and Chapman 2004; Spall 2004; Allen and Durrieu de Madron 2009; Benthuysen et al. 2015; Brink 2016), providing a pathway for water that would otherwise remain trapped on the shelf. Consistent with this mechanism, larger-scale models that include SI parameterizations show enhanced off-shelf transport (Yankovsky et al. 2021), for which the periodic pulsing offers a candidate dynamical explanation.

## 6. Discussion

The PV analysis shows that the topography-aligned frontal structure established by the dense overflow, together with the PV injection by the gravity current impinging along the shelf break, generates the interior PV structure of the overflow and the cross-shelf export of dense water. This has consequences for how overflow regions are represented in ocean models. High-resolution ($\sim 1/10°$) eddy-resolving ocean models capture the broad geometry and pathways of dense overflows and deep western boundary currents, but they do not resolve the small vertical scales and boundary-layer processes that control bottom PV fluxes and the associated instabilities they set up (e.g., Maltrud and McClean 2005; Legg et al. 2009; Danabasoglu et al. 2010; Colombo et al. 2020). The results here suggest that representing these PV fluxes, and the instability responses that follow, may be a prerequisite for quantifying energy exchange, mixing, and cross-shelf transport in global models.

The banded PV structure of the stratified interior (Fig. 8j) resembles that in the previous overflow simulations of Yankovsky and Legg (2019), where thin layers of positive PV also form along the slope above the overflow. The two differ in the PV between the layers, which was negative in that earlier work and taken as evidence of SI, but is near zero here, leaving the interior symmetrically stable. The earlier work attributed the negative PV to frictional destruction adjacent to the slope (Yankovsky and Legg 2019), whereas directly diagnosing the PV boundary fluxes here reveals a

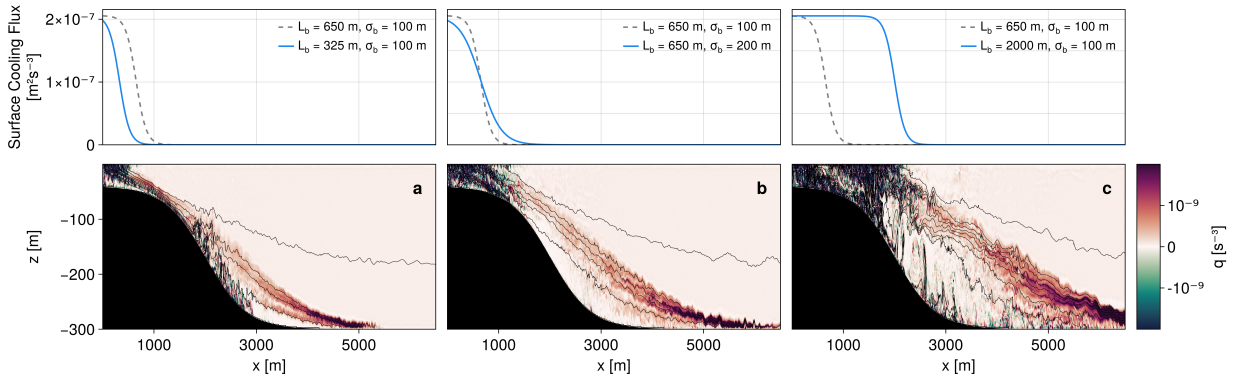



FIG. 14. Snapshots at $t = 20T_f$ of PV from 2D simulations where the surface cooling length scales are varied, demonstrating that the elevated interior PV is robust to these changes. The top row shows the surface buoyancy flux profile for each simulation (blue) compared to the main simulation used throughout this paper (dashed gray), where $L_b$ marks the center of the logistic decay and $\sigma_b$ controls the transition width. (a) The cooling range extends only half as far across the shelf compared to the main setup. (b) The cooling extent is unchanged but the transition width is doubled, giving a smoother decay. (c) The cooling range is greatly extended past the shelf break.

positive frictional injection of PV along the shelf break (Fig. 7a,c). The grid resolution employed in the earlier simulations likely limits the representation of the boundary-layer processes controlling these fluxes, potentially preventing the capture of this positive injection. An accurate representation of the BBL and its interaction with the gravity current thus appears important for obtaining a reliable interior PV signature. Variations in bottom injection and destruction of PV have been linked to current speed and topographic structure (Benthuysen and Thomas 2012; Falcini and Salusti 2015; Gula et al. 2015), and the negative PV anomalies found in other simulations could also reflect genuine differences in the structure, speed, or pulsing frequency of gravity currents impinging on the shelf break. The robustness of the high-PV cap seen here was confirmed by a set of 2D simulations (Fig. 14), where varying the surface buoyancy flux cooling length scales, both in extent and transition width, consistently produces the same high-PV structures. This consistency indicates that the high-PV capping is a general feature of these overflow configurations rather than a consequence of the specific forcing used in the main analysis. Because the interior is symmetrically stable throughout the simulation, the banded shear features found there do not indicate active SI; the

companion paper develops the alternative interpretation that they are signatures of NIWs interacting with this PV structure (Whitley et al. 2026).

These simulations do, however, exhibit SI on the shelf, where its main impact appears to be on cross-shelf exchange. SI organizes into propagating slantwise overturning cells that generate coherent dense pulses traveling toward the shelf break, producing episodic export events synchronized with the SI propagation timescale (Figs. 12, 13). In wider 3D domains, baroclinic eddies provide an additional and potentially dominant pathway for cross-isobath transport (Gawarkiewicz and Chapman 1995; Yankovsky and Legg 2019), though SI signatures persist alongside them. The propagation of SI cells and their role in cross-shelf export has received little attention, yet the low-PV conditions and strong frontal structure characteristic of dense overflow regions suggest this mechanism may be broadly relevant. Consistent with this, larger-scale models that include SI parameterizations exhibit significantly enhanced off-shelf transport (Yankovsky et al. 2021), though the episodic, pulse-driven character of that export and its dynamical link to propagating SI cells is not explicitly represented in such schemes. Whether the propagating cells and pulse-driven export identified here survive in the presence of an active eddy field, or are reorganized by it, remains an open question.

Taken together, these results identify bottom PV fluxes as a leading control on the interior PV structure and on the SI-driven cross-shelf export of dense water. By modifying the background stratification and PV structure, dense overflows create conditions that favor sustained, SI-driven transport of dense water off the shelf; the same PV structure also governs the near-inertial wave interactions examined in the companion paper (Whitley et al. 2026). These mechanisms may link small-scale boundary processes to larger-scale water-mass transformation along deep western boundary currents. Existing SI parameterizations (Yankovsky et al. 2021) can be used to evaluate the role of these processes in dense off-shelf transport and mixing in coarser and more realistic simulations.

## 7. Conclusion

A three-dimensional LES, and an accompanying two-dimensional PV budget, were used to examine how submesoscale dynamics emerge in the formation and adjustment of a dense overflow.

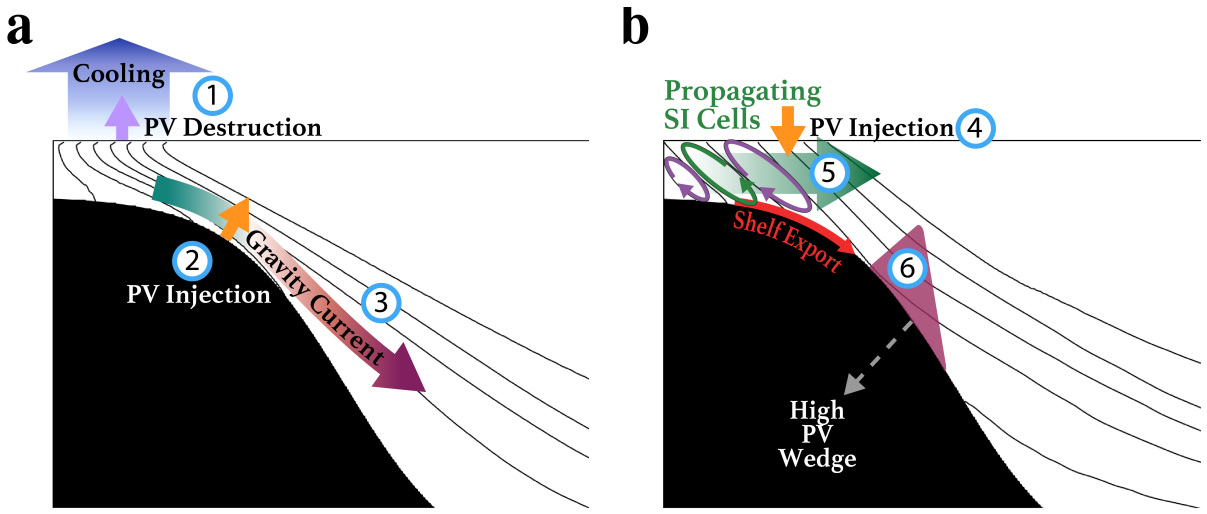



FIG. 15. Schematic of dense overflow processes (a) during cooling and (b) after cooling is shut down. Numbers in blue circles will be used to reference different regions and processes in section 7.

The schematic in Fig. 15 integrates the key elements discussed in this work that will be summarized below. Different regions and processes will be referenced using the numbers marked by blue circles.

The simulated overflow exhibited behavior consistent with observational and numerical studies of dense overflows (Gawarkiewicz and Chapman 1995; Muench and Gordon 1995; Girton et al. 2001; Beaird et al. 2013; Yankovsky and Legg 2019; Lin et al. 2020). Surface cooling generated gravitationally unstable shelf water that cascaded downslope and equilibrated at depth, forming a region of negative along-slope flow ($v < 0$), with a compensating return flow at the surface ($v > 0$) as seen in previous work (Fig. 8a,b; Gawarkiewicz and Chapman 1995; Yankovsky and Legg 2019). Diabatic PV destruction from the surface cooling resulted in a negative PV anomaly on the shelf (Fig. 15a, region 1). Large subinertial dense pulses, formed during cooling, flowed down the topography in the form of gravity currents (Fig. 15a, region 3), generating a frictional PV injection where they impinged along the shelf break (Fig. 15a, region 2).

The negative PV anomaly left behind by surface cooling (Fig. 15a, region 1) rendered the shelf susceptible to SI. After cooling ceased, SI cells propagated towards the shelf break (Fig. 15b, region 5) due to the across-slope gradient in the vertical shear (Pedlosky 2014), with convergent regions between cells episodically transporting dense water across the slope. As these pulses

reached the shelf break, they detached from the cell structures and descended along the slope, exporting water from the densest buoyancy classes off the shelf (Fig. 13). Periodic dense pulses on the order of a few days in realistic simulations and observations have mostly been attributed to mesoscale variability and seasonal changes in overflow waters upstream (Girton and Sanford 2003; von Appen et al. 2014; Almansi et al. 2017), or to topographic Rossby waves propagating along the slope (Geyer et al. 2006; Darelius et al. 2011), but here we identify a submesoscale-driven transport process that actively supports subinertial off-shelf export in dense overflow environments where SI is believed to occur (Allen and Newberger 1996; Magaldi et al. 2011; Yankovsky et al. 2021; Zhou et al. 2022; Goldsworth et al. 2024).

SI-driven cross-shelf export along overflow pathways warrants further investigation in more realistic settings. The present domain size is much smaller than the Rossby deformation radius in the along-isobath direction, limiting the formation of baroclinic eddies, which are often prevalent in dense overflows (Smith 1976; Whitehead et al. 1990; Cenedese et al. 2004; Magaldi et al. 2011; Yankovsky and Legg 2019). Expanding the shelf and domain in more realistic simulations would permit eddy activity near the shelf-break front while also generating regions susceptible to SI, potentially modifying the efficiency of cross-shelf export and the interior PV structure. Sustained observations near overflow pathways, resolving the near-bottom PV structure, would test whether these mechanisms operate as diagnosed here.

In the stratified interior, the PV injected at the shelf break was advected along the bottom topography and persisted as layered PV structures, setting up conditions fundamentally different from those on the shelf. Frontal adjustment after cooling injected additional PV at the top of the shelf-break front (Fig. 15b, region 4), forming a high-PV wedge along the bottom just past the shelf break (Fig. 15b, region 6). The increase in PV in this feature over time could be due to continued frictional injection at the surface or from the diabatic flux associated with the upslope return flow along topography just after the shelf break (Fig. 7b). Due to these injections of positive PV (Figs. 15a, region 2, 15b, region 4), the interior is stable with respect to SI, with susceptibility limited to the shelf (Fig. 8d,j). This interior PV structure is consistent with hydrographic observations across Denmark Strait, where the total Ertel PV largely follows the stratification: weakly stratified, low-PV overflow water lies beneath a strongly stratified layer of elevated PV, with negative PV confined to the steep frontal zone between them (Lin et al. 2020). By setting the interior PV structure

and preconditioning the shelf for SI, boundary PV fluxes can substantially modify dense overflow dynamics, enhancing off-shelf export and contributing to deep-water transformation along some of the most important pathways of the global overturning circulation. The same interior PV structure also points to a dynamical interpretation of the shear bands found along the deep boundary current as the signature of NIWs interacting with the baroclinic flow, rather than SI, which is the subject of the companion paper (Part II, Whitley et al. 2026).

*Acknowledgments.* This material is based upon work supported by the National Science Foundation under Grants OCE-2232441, OCE-2342990, and OCE-2342991. We would like to acknowledge computing support from the Casper system (https://ncar.pub/casper) provided by the NSF National Center for Atmospheric Research (NCAR), sponsored by the National Science Foundation.

*Data availability statement.* Model configuration and analysis scripts will be publicly available at https://github.com/whitleyv/DenseOverflow.

## APPENDIX

### Closure of the PV Budget

The PV budget is evaluated from the boundary fluxes that drive net changes in the volume-integrated PV, but closing it in a turbulent system requires high-temporal-resolution output that was found to be computationally prohibitive in the full 3D domain. Therefore, the PV analysis was conducted in a 2D domain of $(L_x, L_z) = (8000, 300)$ m, with output saved every 60 s. The bulk PV evolution in the 2D domain closely follows that from the 3D domain (Fig. 6), consistent with the shallow along-isobath ($y$) extent of the 3D configuration. Thus, a 2D PV budget provides meaningful insight into the 3D dynamics while allowing the higher time resolution the budget requires.

The PV budget follows from the governing equations (3-5), and is often written as

$$\frac{\partial q}{\partial t} = -\nabla \cdot \boldsymbol{J} = -\nabla \cdot \Big( \underbrace{\boldsymbol{u} q}_{\text{Adv}} - \underbrace{\boldsymbol{\omega}_a \mathscr{D}}_{\text{Diab}} - \underbrace{\boldsymbol{F} \times \nabla b}_{\text{Fric}} \Big), \tag{A1}$$

where the PV can evolve due to advection (Adv), diabatic (Diab), or friction (Fric) "$\boldsymbol{J}$-fluxes". In a 2D system, where all fields are assumed to be uniform in $y$, $\boldsymbol{J}$ can also be written as

$$\boldsymbol{J} = \Big( \nabla b \times \frac{\partial \boldsymbol{u}}{\partial t} \Big) - \boldsymbol{\omega}_a \frac{\partial b}{\partial t} \tag{A2}$$

(Schär 1993; Marshall et al. 2001). Extensive testing here showed that (A2) is better numerically for closing the PV budget since the buoyancy and velocity tendency terms include any nonconservative numerical terms implicitly. With some minimal rearrangement, the frictional and diabatic fluxes

defined in section 4 can be written as

$$\text{Fric} \equiv -\boldsymbol{F} \times \nabla b = (\nabla b \times \frac{\partial \boldsymbol{u}}{\partial t}) + \boldsymbol{A}, \tag{A3}$$

$$\text{Diab} \equiv -\boldsymbol{\omega}_a \mathscr{D} = -\boldsymbol{\omega}_a \frac{\partial b}{\partial t} - \boldsymbol{A} \tag{A4}$$

where $\boldsymbol{A} = \omega_a^x w \frac{\partial b}{\partial z}\hat{\boldsymbol{i}} + \omega_a^z u \frac{\partial b}{\partial x}\hat{\boldsymbol{k}}$ is the PV flux due to vertical (horizontal) advection of the vertical (horizontal) buoyancy gradient acting on the cross-isobath (vertical) component of the absolute vorticity. While (A2) was used to calculate the PV budget due to its inclusion of all resolved and implicit numerical processes, the discussion in section 4 used the classical frictional and diabatic terms to explain the evolution of PV in the simulation, since they are equivalent.

Taking the integral over a fixed volume, $V$, and assuming no advection through the boundary, $\partial V$,

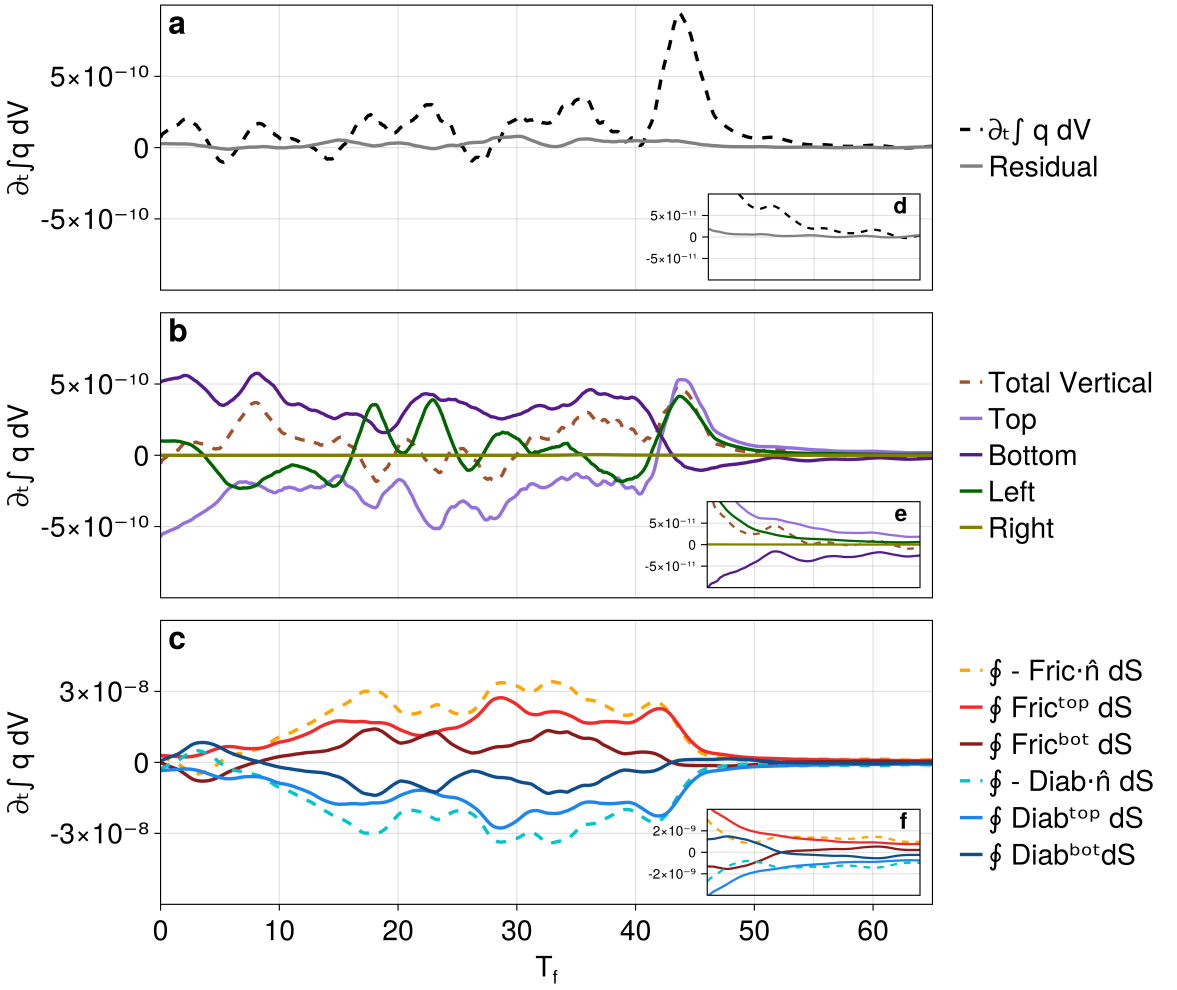
$$\frac{\partial}{\partial t}\int_V q\big|_{2D}\, dV = \oint_{\partial V} -\Big(\text{Fric} + \text{Diab}\Big) \cdot \hat{\boldsymbol{n}}\, dS. \tag{A5}$$

With the definitions in (A3, A4), (A5) makes explicit that a net PV tendency can arise only from boundary fluxes that change the buoyancy or velocity. Expanding (A5), with the frictional and diabatic formulation,

$$\int \frac{\partial q}{\partial t}\Big|_{2D} dV = \oint_{\partial V} \Big( \underbrace{\big(-\frac{\partial v}{\partial z}\mathscr{D}\big)\hat{n}_x}_{\text{Diab}_x} + \underbrace{\big(\frac{\partial b}{\partial z}F^y\big)\hat{n}_x}_{\text{Fric}_x} + \underbrace{\big((f+\frac{\partial v}{\partial x})\mathscr{D}\big)\hat{n}_z}_{\text{Diab}_z} + \underbrace{\big(-\frac{\partial b}{\partial x}F^y\big)\hat{n}_z}_{\text{Fric}_z} \Big)\, dS, \tag{A6}$$

where $\langle \hat{n}_x, \hat{n}_z \rangle$ is positive (negative) for fluxes from the top (bottom) and right (left) boundaries. The four terms in (A6) are labeled by whether they are a diabatic or frictional contribution and whether they are a flux from the horizontal or vertical boundaries. The vertical ($z$) fluxes correspond to the top and bottom contributions denoted by superscripts in section 4.

Evaluating (A6) over the simulation gives the volume-integrated PV tendency in Fig. A1a. Consistent with the total PV evolution (Fig. 6a), the tendency is net positive during cooling peaking sharply at $t = 43T_f$. After cooling ceases, the net rate of PV injection is much smaller and steadily decreasing but remains positive throughout (Fig. A1d). The residual of the budget indicates a small underrepresentation of the volume-integrated PV evolution, with a mean of $2.7\times10^{-11}$ m$^2$s$^{-4}$ during cooling and $4.6\times10^{-12}$ m$^2$s$^{-4}$ afterward (Fig. A1a). This is well below




719 FIG. A1. Evolution of the volume integrated PV along with the components of the budget from (A6). (a) rate
720 of change of PV (black, dashed) calculated directly from the left-hand side of the PV budget (A6), along with
721 the residual (gray, solid) from the right-hand side of (A6). Terms from the PV budget are divided into (b) the
722 flux contribution of each boundary wall and (c) the friction and diabatic components, as discussed in section 4
723 with total components in (A5). The subplots (d-f) cover the time period where the box sits ($t = 46 - 64\,T_f$), with
724 smaller vertical axes limits, to be able to see the flux contributions after cooling is shut down. All terms have
725 been smoothed using a rolling average with a window length of 3 $T_f$.

732 the corresponding tendency in each phase, confirming that the budget is sufficiently closed and the
733 term-by-term decomposition can be interpreted with confidence.

Both the vertical and left-wall fluxes contribute to the positive tendency (Fig. A1b). The left-wall contribution arises from the return flow above the dense overflow, where geostrophic adjustment drives acceleration along the back wall in regions of negative stratification. There, dense fluid is advected downward into lighter ambient fluid, producing a positive Lagrangian buoyancy change and therefore a positive diabatic flux. Although the integrated left-wall flux is comparable in magnitude, its entry point at the closed back wall of the domain is an artificial boundary set by the idealized geometry of the simulation. The top and bottom fluxes, by contrast, act along the physical boundaries of the overflow and set the interior high-PV features and the low shelf PV through the competing injection and destruction of PV along the slope and shelf. Section 4 therefore focuses on their local patterns.

The decomposition of the vertical fluxes confirms the mechanisms identified in section 4 (Fig. A1b,c). During cooling, the net positive tendency is driven by the bottom frictional flux, which dominates the vertical contributions and outweighs the surface diabatic destruction (Fig. A1b,c), consistent with the shelf-break injection of high PV by the passing gravity current. As cooling shuts down, the sharp peak in the tendency at frontal adjustment (40–45$T_f$) corresponds to an increase in the surface frictional flux, confirming that this term builds the high-PV wedge at the shelf break. This surface frictional injection persists, though less dramatically, through the remainder of the simulation (Fig. A1d-f), sustaining the wedge after the initial adjustment. These results confirm that the budget reliably captures the boundary fluxes governing the PV evolution in section 4.

## References


Allen, J. S., and P. A. Newberger, 1996: Downwelling circulation on the oregon continental shelf. part i: Response to idealized forcing. *Journal of Physical Oceanography*, **26**, https://doi.org/10.1175/1520-0485(1996)026⟨2011:DCOTOC⟩2.0.CO;2.

Allen, S. E., and X. Durrieu de Madron, 2009: A review of the role of submarine canyons in deep-ocean exchange with the shelf. *Ocean Science*, **5 (4)**, 607–620, https://doi.org/10.5194/os-5-607-2009.

Almansi, M., T. W. N. Haine, R. S. Pickart, M. G. Magaldi, R. Gelderloos, and D. Mastropole, 2017: High-frequency variability in the circulation and hydrography of the denmark strait overflow

762 from a high-resolution numerical model. *Journal of Physical Oceanography*, **47**, 2999–3013,
763 https://doi.org/10.1175/JPO-D-17-0129.1.

764 Beaird, N. L., P. B. Rhines, and C. C. Eriksen, 2013: Overflow waters at the iceland–faroe ridge
765 observed in multiyear seaglider surveys. *Journal of Physical Oceanography*, **43**, 2334–2351,
766 https://doi.org/10.1175/JPO-D-13-029.1.

767 Benthuysen, J., and L. N. Thomas, 2012: Friction and diapycnal mixing at a slope: Boundary
768 control of potential vorticity. *Journal of Physical Oceanography*, **42**, 1509–1523, https://doi.org/
769 10.1175/JPO-D-11-0130.1.

770 Benthuysen, J., L. N. Thomas, and S. J. Lentz, 2015: Rapid generation of upwelling at a shelf
771 break caused by buoyancy shutdown. *Journal of Physical Oceanography*, **45 (1)**, 294–312,
772 https://doi.org/10.1175/JPO-D-14-0104.1.

773 Brearley, J. A., R. S. Pickart, H. Valdimarsson, S. Jonsson, R. W. Schmitt, and T. W. Haine, 2012:
774 The east greenland boundary current system south of denmark strait. *Deep Sea Research Part*
775 *I: Oceanographic Research Papers*, **63**, 1–19, https://doi.org/https://doi.org/10.1016/j.dsr.2012.
776 01.001.

777 Brink, K., 2016: Cross-shelf exchange. *Annual Review of Marine Science*, **8 (Volume 8, 2016)**,
778 59–78, https://doi.org/https://doi.org/10.1146/annurev-marine-010814-015717.

779 Brink, K. H., and D. A. Cherian, 2013: Instability of an idealized tidal mixing front: Symmetric
780 instabilities and frictional effects. *Journal of Marine Research*, **71**, 425–450, https://doi.org/
781 10.1357/002224013812587582.

782 Bullister, J. L., M. Rhein, and C. Mauritzen, 2013: *Chapter 10 - Deepwater Formation*, Vol.
783 103, 227–253. Academic Press, https://doi.org/https://doi.org/10.1016/B978-0-12-391851-2.
784 00010-6, URL https://www.sciencedirect.com/science/article/pii/B9780123918512000106.

785 Cenedese, C., J. A. Whitehead, T. A. Ascarelli, and M. Ohiwa, 2004: A dense current flowing
786 down a sloping bottom in a rotating fluid. *Journal of Physical Oceanography*, **34**, 188–203.

787 Chafik, L., J. Nilsson, T. Rossby, and A. K. Soman, 2023: The faroe-shetland channel jet:
788 Structure, variability, and driving mechanisms. *Journal of Geophysical Research: Oceans*,
789 **128**, https://doi.org/10.1029/2022JC019083.

790 Chor, T., J. O. Wenegrat, and J. Taylor, 2022: Insights into the mixing efficiency of subme-
791 soscale centrifugal–symmetric instabilities. *Journal of Physical Oceanography*, **52**, 2273–2287,
792 https://doi.org/10.1175/JPO-D-21-0259.1.

793 Colombo, P., and Coauthors, 2020: Representation of the denmark strait overflow in a z -coordinate
794 eddying configuration of the nemo (v3.6) ocean model: resolution and parameter impacts.
795 *Geoscientific Model Development*, **13**, 3347–3371, https://doi.org/10.5194/gmd-13-3347-2020.

796 Danabasoglu, G., W. G. Large, and B. P. Briegleb, 2010: Climate impacts of parameterized
797 nordic sea overflows. *Journal of Geophysical Research: Oceans*, **115**, https://doi.org/10.1029/
798 2010JC006243.

799 Darelius, E., I. Fer, and D. Quadfasel, 2011: Faroe bank channel overflow: Mesoscale variability.
800 *Journal of Physical Oceanography*, **41 (11)**, 2137–2154, https://doi.org/10.1175/JPO-D-11-035.
801 1.

802 Dickson, R. R., and J. Brown, 1994: The production of north atlantic deep water: Sources, rates,
803 and pathways. *Journal of Geophysical Research: Oceans*, **99**, 12 319–12 341, https://doi.org/
804 10.1029/94JC00530.

805 Evans, D. G., N. P. Holliday, S. Bacon, and I. L. Bras, 2022: Mixing and air-sea buoyancy fluxes
806 set the time-mean overturning circulation in the subpolar north atlantic. *EGUsphere*, 1–36,
807 https://doi.org/10.5194/egusphere-2022-1059.

808 Falcini, F., and E. Salusti, 2015: Friction and mixing effects on potential vorticity for bottom
809 current crossing a marine strait: An application to the sicily channel (central mediterranean sea).
810 *Ocean Science*, **11**, 391–403, https://doi.org/10.5194/os-11-391-2015.

811 Gawarkiewicz, G., and D. C. Chapman, 1995: A numerical study of dense water formation and
812 transport on a shallow, sloping continental shelf. *Journal of Geophysical Research: Oceans*,
813 **100**, 4489–4507, https://doi.org/10.1029/94JC01742.

814 Geyer, F., S. Østerhus, B. Hansen, and D. Quadfasel, 2006: Observations of highly regular oscil-
815 lations in the overflow plume downstream of the Faroe Bank Channel. *Journal of Geophysical*
816 *Research*, **111**, C12 020, https://doi.org/10.1029/2006JC003693.

Girton, J. B., and T. B. Sanford, 2003: Descent and modification of the overflow plume in the denmark strait *. *Journal of Physical Oceanography*, **33**, 1351–1364, https://doi.org/GirtonSanford2003.

Girton, J. B., T. B. Sanford, and R. H. Käse, 2001: Synoptic sections of the denmark strait overflow. *Geophysical Research Letters*, **28**, 1619–1622, https://doi.org/10.1029/2000GL011970.

Goldsworth, F. W., H. L. Johnson, D. P. Marshall, and I. A. L. Bras, 2024: Destratifying and restratifying instabilities during down-front wind events: A case study in the irminger sea. *Journal of Geophysical Research: Oceans*, **129**, https://doi.org/10.1029/2023JC020365.

Gula, J., M. J. Molemaker, and J. C. McWilliams, 2015: Topographic vorticity generation, submesoscale instability and vortex street formation in the gulf stream. *Geophysical Research Letters*, **42**, 4054–4062, https://doi.org/10.1002/2015GL063731.

Haine, T. W. N., and J. Marshall, 1998: Gravitational, symmetric, and baroclinic instability of the ocean mixed layer. *Journal of Physical Oceanography*, **28**, 634–658, https://doi.org/10.1175/1520-0485(1998)028⟨0634:GSABIO⟩2.0.CO;2.

Haynes, P. H., and M. E. McIntyre, 1987: On the evolution of vorticity and potential vorticity in the presence of diabatic heating and frictional or other forces. *Journal of Atmospheric Sciences*, **44 (5)**, 828 – 841, https://doi.org/10.1175/1520-0469(1987)044⟨0828:OTEOVA⟩2.0.CO;2.

Huthnance, J. M., 1995: Circulation, exchange and water masses at the ocean margin: the role of physical processes at the shelf edge. *Progress in Oceanography*, **35 (4)**, 353–431, https://doi.org/https://doi.org/10.1016/0079-6611(95)80003-C.

Ivanov, V. V., G. I. Shapiro, J. M. Huthnance, D. L. Aleynik, and P. N. Golovin, 2004: Cascades of dense water around the world ocean. *Progress in Oceanography*, **60 (1)**, 47–98, https://doi.org/10.1016/j.pocean.2003.12.002.

Killworth, P. D., 1983: Deep convection in the world ocean. *Reviews of Geophysics*, **21**, 1–26, https://doi.org/10.1029/RG021i001p00001.

Koszalka, I. M., T. W. N. Haine, and M. G. Magaldi, 2013: Fates and travel times of denmark strait overflow water in the irminger basin*. *Journal of Physical Oceanography*, **43**, 2611–2628, https://doi.org/10.1175/JPO-D-13-023.s1.

Köhl, A., R. H. Käse, D. Stammer, and N. Serra, 2007: Causes of changes in the denmark strait overflow. *Journal of Physical Oceanography*, **37**, 1678–1696, https://doi.org/10.1175/JPO3080.1.

Le Bras, I. A.-A., J. Callies, F. Straneo, T. C. Biló, J. Holte, and H. L. Johnson, 2022: Slantwise convection in the irminger sea. *Journal of Geophysical Research: Oceans*, **127**, https://doi.org/10.1029/2022JC019071.

Legg, S., 2012: *Overflows and Convectively Driven Flows*, 203–235. Cambridge University Press.

Legg, S., and Coauthors, 2009: Improving oceanic overflow representation in climate models: The gravity current entrainment climate process team. *Bulletin of the American Meteorological Society*, **90**, https://doi.org/10.1175/2008BAMS2667.I.

Lentz, S. J., and D. C. Chapman, 2004: The importance of nonlinear cross-shelf momentum flux during wind-driven coastal upwelling. *Journal of Physical Oceanography*, **34 (11)**, 2444–2457, https://doi.org/10.1175/JPO2644.1.

Lin, P., R. S. Pickart, K. Jochumsen, G. W. K. Moore, H. Valdimarsson, T. Fristedt, and L. J. Pratt, 2020: Kinematic structure and dynamics of the denmark strait overflow from ship-based observations. *Journal of Physical Oceanography*, **50**, 3235–3251, https://doi.org/10.1175/JPO-D-20-0095.1.

Lumpkin, R., and K. Speer, 2007: Global ocean meridional overturning. *Journal of Physical Oceanography*, **37**, 2550–2562, https://doi.org/10.1175/JPO3130.1.

MacCready, P., and P. B. Rhines, 1991: Buoyant inhibition of ekman transport on a slope and its effect on stratified spin-up. *Journal of Fluid Mechanics*, **223**, 631–661, https://doi.org/10.1017/S0022112091001581.

Magaldi, M. G., and T. W. Haine, 2015: Hydrostatic and non-hydrostatic simulations of dense waters cascading off a shelf: The east greenland case. *Deep-Sea Research Part I: Oceanographic Research Papers*, **96**, 89–104, https://doi.org/10.1016/j.dsr.2014.10.008.

Magaldi, M. G., T. W. N. Haine, and R. S. Pickart, 2011: On the nature and variability of the east greenland spill jet: A case study in summer 2003*. *Journal of Physical Oceanography*, **41**, https://doi.org/10.1175/JPO-D-10.

873 Maltrud, M. E., and J. L. McClean, 2005: An eddy resolving global 1/10° ocean simulation. *Ocean*
874 *Modelling*, **8**, 31–54, https://doi.org/10.1016/j.ocemod.2003.12.001.

875 Marshall, J., D. Jamous, and J. Nilsson, 2001: Entry, flux, and exit of potential vorticity in
876 ocean circulation. *Journal of Physical Oceanography*, **31**, 777–789, https://doi.org/10.1175/
877 1520-0485(2001)031⟨0777:EFAEOP⟩2.0.CO;2.

878 Muench, R. D., and A. L. Gordon, 1995: Circulation and transport of water along the western wed-
879 dell sea margin. *Journal of Geophysical Research: Oceans*, **100**, 18 503–18 515, https://doi.org/
880 10.1029/95JC00965.

881 Naveira Garabato, A. C., and Coauthors, 2019: Rapid mixing and exchange of deep-ocean waters
882 in an abyssal boundary current. *Proceedings of the National Academy of Sciences*, **116**, 13 233–
883 13 238, https://doi.org/10.1073/pnas.1904087116.

884 Pedlosky, J., 2014: Symmetric instability of cross-stream varying currents. *Journal of Marine*
885 *Research*, **72**, 31–45.

886 Saberi, A., T. W. N. Haine, R. Gelderloos, M. F. de Jong, H. Furey, and A. Bower, 2020: Lagrangian
887 perspective on the origins of denmark strait overflow. *Journal of Physical Oceanography*, **50**,
888 2393–2414, https://doi.org/10.1175/JPO-D-19-0210.1.

889 Schär, C., 1993: A generalization of bernoulli's theorem. *Journal of the Atomspheric Sciences*, **50**,
890 1437–1443.

891 Shapiro, G. I., and A. E. Hill, 1997: Dynamics of dense water cascades at the shelf edge. *Jour-*
892 *nal of Physical Oceanography*, **27 (11)**, 2381–2394, https://doi.org/10.1175/1520-0485(1997)
893 027⟨2381:DODWCA⟩2.0.CO;2.

894 Smith, P. C., 1976: Baroclinic instability in the denmark strait overflow. *Journal of Physical*
895 *Oceanography*, **6**, 355–371, https://doi.org/10.1175/1520-0485(1976)006⟨0355:BIITDS⟩2.0.
896 CO;2.

897 Spall, M. A., 2004: Boundary currents and watermass transformation in marginal seas. *Jour-*
898 *nal of Physical Oceanography*, **34 (5)**, 1197–1213, https://doi.org/10.1175/1520-0485(2004)
899 034⟨1197:BCAWTI⟩2.0.CO;2.

Taylor, J. R., and R. Ferrari, 2009: On the equilibration of a symmetrically unstable front via a secondary shear instability. *Journal of Fluid Mechanics*, **622**, 103–113, https://doi.org/10.1017/S0022112008005272.

Thomas, L. N., J. R. Taylor, R. Ferrari, and T. M. Joyce, 2013: Symmetric instability in the gulf stream. *Deep Sea Research Part II: Topical Studies in Oceanography*, **91**, 96–110, https://doi.org/10.1016/j.dsr2.2013.02.025.

Thorpe, A. J., and R. Rotuno, 1989: Nonlinear aspects of symmetric instability. *J. Atmos. Sci.*, **46**, 1285–1299, https://doi.org/10.1175/1520-0469(1989)046⟨1285:NAOSI⟩2.0.CO;2.

von Appen, W.-J., R. S. Pickart, K. H. Brink, and T. W. Haine, 2014: Water column structure and statistics of denmark strait overflow water cyclones. *Deep Sea Research Part I: Oceanographic Research Papers*, **84**, 110–126, https://doi.org/10.1016/j.dsr.2013.10.007.

Wagner, G. L., and Coauthors, 2025: High-level, high-resolution ocean modeling at all scales with oceananigans. *arXiv preprint (JAMES tbd)*.

Wenegrat, J. O., and L. N. Thomas, 2020: Centrifugal and symmetric instability during ekman adjustment of the bottom boundary layer. *Journal of Physical Oceanography*, **50**, 1793–1812, https://doi.org/10.1175/JPO-D-20-0027.1.

Whitehead, J. A., M. E. Stern, G. R. Flierl, and B. A. Klinger, 1990: Experimental observations of baroclinic eddies on a sloping bottom. *Journal of Geophysical Research: Oceans*, **95**, 9585–9610, https://doi.org/10.1029/JC095iC06p09585.

Whitley, V., J. Wenegrat, and L. Thomas, 2026: Submesoscale dynamics of dense overflows. Part II: Near-inertial wave trapping and reflection, Journal of Physical Oceanography, submitted.

Whitley Clark, V., 2026: Internal wave - topography and flow interactions in the bottom boundary layer. Ph.D. thesis, University of Maryland, College Park, 82-130 pp., https://doi.org/10.13016/am4v-rdwy.

Yankovsky, E., and S. Legg, 2019: Symmetric and baroclinic instability in dense shelf overflows. *Journal of Physical Oceanography*, **49**, 39–61, https://doi.org/10.1175/JPO-D-18-0072.1.

Yankovsky, E., S. Legg, and R. Hallberg, 2021: Parameterization of submesoscale symmetric instability in dense flows along topography. *Journal of Advances in Modeling Earth Systems*, **13**, https://doi.org/10.1029/2020MS002264.

Zhou, H., W. Dewar, W. Yang, H. Liu, X. Chen, R. Li, C. Liu, and G. Gopalakrishnan, 2022: Observations and modeling of symmetric instability in the ocean interior in the northwestern equatorial pacific. *Communications Earth & Environment*, **3**, 28, https://doi.org/10.1038/s43247-022-00362-4.